Annexin A1 is a polarity cue that directs planar mitotic spindle orientation during mammalian epithelial morphogenesis

Maria Fankhaenel[1,2], Farahnaz Sadat Golestan Hashemi[1,2], Larissa Mourao[3], Emily Lucas[1,2], Manal Mosa Hosawi[1,2], Paul Skipp[1,2,4], Xavier Morin[5], Colinda L.G.J. Scheele[3] and Salah Elias[1,2*]

[1]School of Biological Sciences, University of Southampton, Southampton, SO17 1BJ, United Kingdom

[2]Insitute for Life Sciences, University of Southampton, Southampton, SO17 1BJ, United Kingdom

[3]VIB-KULeuven Center for Cancer Biology, Herestraat 49, 3000, Leuven, Belgium

[4]Centre for Proteomic Research, University of Southampton, Southampton, SO17 1BJ, United Kingdom

[5]Ecole Normale Supérieure, CNRS, Inserm, Institut de Biologie de l'Ecole Normale Supérieure (IBENS), PSL Research University, Paris, France

*Correspondence: s.k.elias@soton.ac.uk

Abstract

Oriented cell divisions are critical for the formation and maintenance of structured epithelia. Proper mitotic spindle orientation relies on polarised anchoring of force generators to the cell cortex by the evolutionarily conserved $G_{\alpha i}$-LGN-NuMA complex. However, the polarity cues that control cortical patterning of this ternary complex remain largely unknown in mammalian epithelia. Here we identify the membrane-associated protein Annexin A1 (ANXA1) as a novel interactor of LGN in mammary epithelial cells. ANXA1 acts independently of $G_{\alpha i}$ to instruct the accumulation of LGN and NuMA at the lateral cortex to ensure cortical anchoring of Dynein-Dynactin and astral microtubules and thereby planar alignment of the mitotic spindle. Loss of ANXA1 randomises mitotic spindle orientation, which in turn disrupts epithelial architecture and luminogenesis in three-dimensional cultures of primary mammary epithelial cells. Our findings establish ANXA1 as an upstream cortical cue that regulates LGN to direct planar cell divisions during mammalian epithelial morphogenesis.

Introduction

Oriented cell divisions (OCDs) represent a fundamental mechanism for epithelial tissue morphogenesis, repair and differentiation during development and homeostasis [1]. Disruption in OCDs has direct implications for developmental disorders and cancer [2]. OCDs are defined by the orientation of the mitotic spindle, which in turn determines the position and fate of daughter cells in epithelial tissues [1, 3]. The evolutionarily conserved ternary complex formed by the $G_{\alpha i}$ subunit of heterotrimeric G proteins, the nuclear mitotic apparatus protein (NuMA) and LGN (also known as GPSM2), are essential regulators that polarise force generators and capture astral microtubules at the cell cortex to orient the mitotic spindle [4]. During mitosis, LGN is recruited to the cell cortex through the interaction of its carboxy-terminal GoLoco motifs with GDP-bound $G_{\alpha i}$, which is anchored at the plasma membrane through myristoylation. The N-terminal tetratricopeptide repeat (TPR) domain of LGN interacts with NuMA that is released in the cytoplasm upon nuclear-envelope breakdown [4]. Polarised cortical localisation of the $G_{\alpha i}$-LGN-NuMA complex is crucial for the interaction of NuMA with astral microtubules and recruitment of the Dynein-Dynactin motor complex through direct NuMA binding, which triggers minus-end directed movement of Dynein, generating pulling forces on astral microtubules that position and orient the mitotic spindle [5]. $G_{\alpha i}$ subunits have a default distribution throughout the whole cell surface and do not contribute to the polarisation of LGN at cortical crescents facing the spindle poles [6]. The mechanisms that polarise LGN at the cell cortex remain unfolding.

The orientation of the mitotic spindle in epithelia is instructed by polarity cues that translate external signals to pattern cortical LGN. The core members of the Par polarity complex (Par3, atypical protein kinase C (aPKC), and Par6), were shown to play a key role in nearly every instance of OCDs [3, 4, 7]. In *Drosophila* neuroblasts, establishment of an apico-basal polarity axis allows the adapter protein Inscuteable (Insc) to accumulate at the apical cortex, where it binds to Par3, facilitating apical recruitment of LGN to form a ternary complex that orients the mitotic spindle perpendicularly to the epithelial surface [8, 9]. Through the same mechanism, mammalian Insc (mInsc) controls perpendicular divisions in the mouse embryonic epidermis

to promote stratification [10]. Combined loss of $G_{\alpha i}$ and mInsc in the murine epidermis results in a shift towards planar divisions, suggesting that these occur by default in the absence of apical polarity cues [10]. Nonetheless, studies in canine kidney MDCK cells showed that phosphorylation of LGN by apical aPKC mediates its exclusion to the lateral cortex, favouring the planar orientation of the mitotic spindle [11]. Other polarity cues instruct lateral patterning of cortical LGN in mammalian epithelial cells. While E-cadherin, Afadin, Disk large (Dlg) and Ric-8A direct the recruitment of LGN at the lateral cortex [12-16], ABL1 and SAPCD2 act on its cortical accumulation and restriction [17, 18]. These diverse mechanisms that control LGN localisation at restricted cortical domains have also been shown to act in a context-dependent and tissue-specific manner to ensure adequate positioning of cell fate determinants and daughter cells during planar or perpendicular cell divisions.

The mammary gland is a unique organ that develops predominantly after birth and represents a powerful model system to study the mechanisms of adult mammalian epithelial morphogenesis. Postnatal morphogenesis of the mammary gland in response to hormonal stimuli drives dramatic tissue turnover and remodelling during successive pregnancies [19]. The contribution of OCDs to mammary epithelial morphogenesis remains ill-defined [3]. A few studies have shown that Aurora-A kinase (AurkA), Polo-like kinase 2 (Plk2), integrins, stathmin, huntingtin and Slit2/Robo1, control mitotic spindle orientation in mammary epithelial cells (MECs) [20-25]. So far, only huntingtin and Slit2/Robo1 were reported to regulate cortical localisation of LGN in the mammary epithelium [22, 25]. Recent evidence strongly suggests that OCDs affect cell fate outcomes in mammary stem/progenitor cells [3, 24, 26], and their dysregulation is linked to breast cancer development and aggressiveness [3, 24, 26, 27]. Thus, unravelling the molecular components and precise mechanisms of mitotic spindle orientation in the mammary epithelium remains an important priority.

Here we exploit affinity purification and mass spectrometry methods to characterise the cortical interactome of LGN in mitotic MECs. We identify Annexin A1 (ANXA1), a potent membrane-associated immunomodulatory protein [28], as a novel LGN interactor that has not been reported previously to play any function in cell division. We demonstrate that ANXA1

interacts with LGN to restrict its distribution to the lateral cell cortex, thereby regulating the dynamic and planar orientation of the mitotic spindle. In addition, we show that ANXA1-mediated regulation of planar division is crucial for epithelial architecture and luminogenesis in three-dimensional (3D) cultures of primary MECs. Collectively, the present experiments establish ANXA1 as a novel key polarity cue that instructs the accumulation of LGN at the lateral cell cortex, providing a mechanism that controls planar cell divisions during mammalian epithelial morphogenesis.

Results

LGN interactome in mitotic MECs

To identify LGN-binding proteins, we generated clonal MCF-10A MECs stably expressing GFP-LGN. GFP-expressing MCF-10A cells were used as controls. GFP-LGN display the same mitosis-dependent cortical localisation as compared to endogenous LGN (Fig S1A) and mitosis progression is not affected by the expression of GFP-LGN (Fig S1B). We used affinity purification to isolate the GFP-LGN complex from cells synchronised in mitosis (arrested in metaphase), and in interphase (arrested in G2 phase) (Supplementary Fig. 1c). We validated synchronisation efficiency by assessing the accumulation of phospho-Histone H3, and cellular distribution of LGN and microtubules (Fig S1D and S1E). Finally, we confirmed that the protocol specifically purifies the exogenous LGN in the GFP-LGN-bead-bound fractions as compared to controls (Fig S1F).

The purified GFP-LGN protein complex was trypsin-digested and analysed using liquid chromatography-tandem mass spectrometry (LC-MS/MS). All mass spectrometry proteomics data obtained from interphase and metaphase cells in two independent experiments have been summarised in Table S1 and deposited to the ProteomeXchange Consortium via the PRIDE partner repository [29]. Removal of proteins represented in the control beads, as well as common MS contaminants using the Contaminant Repository for Affinity Purification (CRAPome) database [30] identified an LGN/GPSM2 protein subnetwork of 18 proteins in metaphase cells (Fig 1A, Table S2). The LGN protein network includes known interactors such as NuMA, INSC and its partner PAR3 (Fig 1A, Table S2). Our data also suggest that NUMB, a key modulator of NOTCH and regulator of asymmetric cell divisions [3], may form a complex with INSC and PAR3. A Gene Ontology (GO) analysis revealed that “spindle organisation”, “establishment of spindle localisation”, “regulation of spindle assembly”, “ciliary basal body-plasma membrane docking”, “spindle assembly”, “regulation of mitotic spindle organisation”, “metaphase plate congression”, “regulation of protein localisation to cell periphery”, “regulation of chromosome segregation”, and “regulation of mitotic sister chromatid segregation”, are the most enriched biological processes, and that the identified proteins are involved in pathways

regulating mitosis progression, centrosome formation and maturation, and microtubule organisation (Fig 1B, Table S2). Several proteins including PLK1, Dynein (DYNC1H1), p150^{Glued} (DCTN2), γ-tubulin (TUBG1), importin-α1 (KPNA2) and RAN, known to form a complex with NuMA to regulate mitotic spindle assembly and orientation, are found in the LGN protein network and co-purify with additional mitotic spindle regulators, namely CLASP1, Cyclin B1 (CCNB1) and HAUS6 [6, 31-46], in the NuMA subnetwork where we also found the oncogene EIF3E [46, 47]. Finally, we identified a ternary complex comprising the membrane-associated protein Annexin A1 (ANXA1) [48] and its partner S100A11 (S100 Ca^{2+}-binding protein A11) [49], as well as the Serum Amyloid A-1 protein (SAA1) [50], that co-purifies with LGN. We decided to gain more insight into this novel interaction. When we performed pull-down assays combined with western blotting analysis, we determined that GFP-LGN precipitates ANXA1 (Fig 1C). Reciprocal immunoprecipitation shows that ANXA1-mCherry co-purifies with LGN (Fig 1D). To further validate the association between ANXA1 and LGN, we used an *in situ* proximity ligation assay (PLA). We detected proximity between ANXA1 and LGN in the cytoplasm and the cell cortex, where the cortical signal was higher in metaphase as compared to interphase (Fig 1E). Taken together these experiments uncover ANXA1 as a previously unknown cortical interactor of LGN in mitotic mammalian epithelial cells.

Cell-cycle-dependent regulation of ANXA1 association with LGN at the cell cortex

Previous studies in post-mitotic epithelial cells established ANXA1 as a cytosolic protein that is recruited to the phospholipids of the plasma membrane and intracellular vesicular organelles, in a Ca^{2+}-dependent manner [51], but no mitosis-specific function has been reported for the protein. We characterised the cell-cycle dependent localisation of ANXA1 in MCF-10A cells by immunofluorescence and confocal imaging. We observed that ANXA1 displays a consistent accumulation at the cell cortex, where it co-localises with LGN, NuMA and S100A11 during mitosis (Fig 1F, Fig S2A). A fraction of ANXA1 redistributes to the cytosol to localise around microtubules throughout mitosis (Fig S2B). We then further assessed the co-distribution of endogenous and ectopically expressed ANXA1 and LGN (Fig 1F, Fig S2C

and S2D). LGN displays a diffuse cytosolic localisation in interphase, whereas ANXA1 is uniformly distributed at the cell cortex (Fig 1G, Fig S2C and S2D). At mitosis entry, LGN relocates to the cell cortex where it colocalises with ANXA1. Consistent with previous studies [6, 52, 53], LGN translocates from the central cortex during prometaphase, to polarise at the lateral cortex at metaphase. In sharp contrast, ANXA1 accumulates at the central cortex during prometaphase, while its amounts at the lateral cortex are lower as compared to LGN (Fig 1F, and 1G, Fig S2C and S2D). Moreover, before the metaphase plate finds a central position, ANXA1 accumulates more at the closest lateral cortex to the chromosomes whereas LGN is more abundant at the opposing distant cortex (Fig 1F). Once chromosomes are aligned centrally in metaphase, LGN distributes equally at the lateral cortex, consistent with previous studies [6], while ANXA1 displays a more uniform, circumferential cortical distribution, a pattern observed until cytokinesis (Fig 1F and 1G, Fig S2C and S2D). Collectively these experiments indicate that the distribution of ANXA1 along with LGN is spatiotemporally regulated during mitosis.

ANXA1 restricts LGN localisation to the lateral cortex during mitosis

LGN orients the mitotic spindle by localising NuMA and Dynein-Dynactin to the cell cortex [3, 4]. To investigate a possible function for ANXA1 in controlling LGN cortical localisation, we performed live imaging and assessed the effect of ANXA1 knockdown on the dynamic distribution of GFP-LGN in MCF-10A cells during mitosis. In cells transfected with a control siRNA (si-Control), we observed that GFP-LGN is recruited to the cell cortex during prometaphase to accumulate bilaterally at the cortex opposite to the spindle poles during metaphase (Fig 2A, Movie S1), consistent with previous studies in HeLa cells [6]. The amounts of cortical GFP-LGN decrease progressively during anaphase, until telophase and cytokinesis where the protein redistributes to the cytosol (Fig 2A). In contrast, siRNA-mediated knockdown of ANXA1 impairs the dynamic distribution of GFP-LGN at the cortex in ~78% of ANXA1-depleted cells (Fig 2A-2C, Movie S2, Movie S3, Movie S4). We found that GFP-LGN remains at the central cortex in 50.37 ± 5.19% of ANXA1-depleted cells, while in 17.78 ± 3.40% the

protein shows a circumferential distribution. Additionally, 10.37 ± 5.79% of ANXA1-depleted cells display a unilateral cortical accumulation of GFP-LGN. We did not find cells negative for cortical GFP-LGN in the absence of ANXA1, allowing us to conclude that ANXA1 acts on LGN restricted accumulation at the lateral cortex, rather than on its recruitment.

Next, we performed immunofluorescence and confocal imaging to evaluate the extent to which ANXA1 affects the ability of LGN to localise NuMA and the p150^{Glued} Dynactin subunit to the lateral cortex during metaphase. In agreement with our live imaging results, ANXA1 knockdown prevents the bilateral cortical accumulation of LGN, with the protein displaying central (si-ANXA1#1: 53.33 ± 7.70%; si-ANXA1#2: 43.02 ± 8.76%), circumferential (si-ANXA1#1: 19.68 ± 3.86%; si-ANXA1#2: 25.7 ± 1.50 %), or unilateral (si-ANXA1#1: 16.51 ± 5.20%; si-ANXA1#2: 14.26 ± 7.20%) distributions in ANXA1-depleted cells (Fig 2D and 2E). Similarly, ANXA1 knockdown impairs NuMA cortical-lateral restriction, which displays a central distribution in a large proportion of ANXA1-depleted cells (si-ANXA1#1: 35.71± 7.14%; si-ANXA1#2: 27.34± 8.77%) (Fig 2D and 2E). By contrast, we found that p150^{Glued} was absent at the cell cortex in the majority (si-ANXA1#1: 48.60 ± 3.01%; si-ANXA1#2: 48.46 ± 0.79%) of ANXA1-depleted cells (Fig 2D and 2E), indicating an impairment in its cortical recruitment. Ectopic expression of ANXA1-mCherry that is si-ANXA1#2-resistant rescues the cortical localisation defects of LGN, NuMA and p150^{Glued}, induced upon depletion of endogenous ANXA1 (Fig 2D-2F). Interestingly, ANXA1 knockdown did not affect $G_{\alpha i}$ cortical distribution (Fig 2G and 2H). Thus, ANXA1 is required to localise the LGN-NuMA-Dynein-Dynactin complex at the lateral cortex during mitosis, independently of $G_{\alpha i}$.

ANXA1 recruitment to the membrane phospholipids is facilitated by its binding to S100A11 [54-56]. This was suggested to be modulated by phosphorylation of ANXA1 by the TRPM7 (transient receptor potential melastatin 7) channel-kinase [57]. To assess the requirement of ANXA1 localisation to the plasma membrane for the polarised cortical accumulation of LGN and NuMA, we treated MCF-10A cells for 2 hours (2h) with 20 μM of TG100-115, a potent TRPM7 kinase inhibitor [58]. Upon TG100-115 treatment, ANXA-S100A11 accumulation at the

plasma membrane is impaired with ANXA1 redistributing uniformly to the cytoplasm during metaphase (Fig 3A and 3B). Similarly to ANXA1 knockdown, this treatment results in an aberrant accumulation of LGN and NuMA at the cell cortex and impairs p150^{Glued} cortical recruitment (Fig 3C and 3D), further indicating that ANXA1 serves as a membrane-associated molecular landmark to ensure proper cortical distribution of LGN and its effectors, NuMA and Dynein-Dynactin, during metaphase.

ANXA1 acts upstream of LGN to regulate mitotic progression and spindle orientation

Proper cortical localisation of the LGN-NuMA-Dynein-Dynactin complex is required to generate polarised pulling forces on astral microtubules that orient the mitotic spindle [4]. The results above strongly suggest that ANXA1 regulates mitotic spindle positioning. To test this possibility, we performed live imaging in control and ANXA1-depleted MCF-10A cells, in which we labelled microtubules with SiR-tubulin [59] and DNA with Hoechst 33342. First, we observed significant defects in the dynamics of cell division in a vast majority of ANXA1-depleted cells (90.95 ± 2.15%) as compared to controls (12.04 ± 2.45%) (Fig 4A and 4B, Movie S5, Movie S6, Movie S7, Movie S8). The proportion of cells that completed mitosis decreases significantly upon ANXA1 knockdown (si-ANXA1#1: 57.14 ± 9.18%, versus si-Control: 100 ± 0.00%) (Fig 4C). In ANXA1-depleted cells that completed mitosis, the duration of the mitotic process is significantly extended as revealed by increased transition time from nuclear envelope breakdown (NEBD) to anaphase onset (si-ANXA1#1: 54.11 ± 1.08 min versus si-Control: 38.56 ± 1.52 min) (Fig 4D). The size and morphology of the mitotic spindle are affected as well, with ~36% and ~14% of ANXA1-depleted cells displaying abnormal bipolar or multipolar spindles, respectively (Fig 4E). Our analyses also reveal that ANXA1 knockdown results in chromosome segregation defects in ~36% of cells (Fig 4E). During metaphase, ~82% of ANXA1-depleted cells display excessive oscillations of the mitotic spindle relative to the z axis between successive time frames, whereas in control cells the spindle does not display notable oscillatory z rotations and remains in a planar position (Fig 4F-4H). We further

confirmed these observations using immunofluorescence and confocal imaging, which shows that virtually all mitotic spindles in the controls orient parallel to the substratum plane (3.87° ± 0.37°), whereas ANXA1-depleted cells display spindle orientation defects (si-ANXA1#1: 15.45° ± 0.77°; si-ANXA1#2: 18.53° ± 2.02°), which are rescued upon ectopic expression of the si-ANXA1#2-resistant ANXA1-mCherry (si-ANXA1#2 + ANXA1-mCherry: 4.6° ± 0.6°) (Fig S3A and S3B). Live imaging experiments also show a significant increase in mitotic spindle oscillatory rotations within the xy plane upon ANXA1 knockdown, with spindle oscillation frequencies significantly higher as compared to controls (Fig 4I-4K). In control cells, mitotic spindles mostly oscillate around their initial position at metaphase onset, whereas ANXA1-depleted cells display random spindle displacements (Fig 4L), where average movements away from the original position are significantly higher as compared to controls (si-ANXA#1: 2.56 ± 0.09 μm versus si-Control: 1.80 ± 0.17 μm) (Fig 4M). Spindle displacement speed was not affected upon ANXA1 depletion (si-ANXA#1: 0.32 ± 0.05 μm/min versus si-Control: 0.27 ± 0.02 μm/min) (Fig 4N). Together, these data indicate that ANXA1 is required for proper mitotic spindle positioning and assembly, faithful chromosome segregation to daughter cells, as well as mitotic progression.

We next tested whether ANXA1 lies upstream of LGN, using immunofluorescence and confocal imaging. Consistent with previous studies [15, 60-62], we found that siRNA mediated LGN knockdown results in mitotic spindle misorientation, with spindle angles αz increasing from 3.14° in controls to 13.80° and 17.21° in cells treated with si-LGN#1 and si-LGN#2, respectively (Fig S3C and S3D). However, LGN depletion does not affect the cortical distribution of ANXA1, whereas it impairs the recruitment of NuMA to the lateral cortex (Fig S3E and S3F). These data allow us to conclude that ANXA1 acts upstream of LGN to control mitotic spindle orientation.

The anchoring of astral microtubules to the cell cortex, and the regulation of their number and stability by the LGN-NuMA-Dynein-Dynactin complex are key to ensure correct mitotic spindle orientation and assembly [4]. We therefore examined microtubule stability and

dynamics upon ANXA1 knockdown in mitotic cells. Using immunofluorescence and confocal imaging, we show that ANXA1 knockdown results in elongation and buckling of astral microtubules, while their overall intensity and number remain unaffected, suggesting an increased stability (Fig S4A-S4C). Astral microtubule elongation and stabilisation correlate with spindle misplacement close to one side of ANXA1-depleted cells, suggesting imbalance in the forces exerted on the mitotic spindle (Fig S4D). These results are in line with our earlier observations showing an increase in mitosis duration and proportion of cells displaying abnormal mitotic spindles in ANXA1-depleted cells. Actin cytoskeleton reorganisation during mitosis into a uniform contractile meshwork at the cell cortex drives the generation of cortical tensions, which are required for accurate mitotic spindle positioning [13, 63, 64]. ANXA1 has been shown to bind and bundle F-actin in a Ca^{2+}-dependent manner, ensuring a dynamic crosstalk between the plasma membrane and the actin cytoskeleton [65]. This prompted us to analyse the consequences of ANXA1 knockdown on cortical actin integrity during metaphase. Phalloidin labelling shows that F-actin organisation is perturbed in ANXA1-depleted cells, leading to a significant reduction in the cortical actin signal (Fig S4E and S4F). Interestingly, treatment of MCF-10A cells with 1 μM of the actin depolymerising drug latrunculin A (Fig S4G) does not affect the localisation of ANXA1 to the plasma membrane, whereas it impairs the recruitment of LGN, NuMA and $p150^{Glued}$ to the cell cortex during metaphase (Fig S4H and S4I). Together, these experiments further sustain the hypothesis that ANXA1 is an upstream cortical cue regulating proper microtubule-cortex crosstalk to ensure accurate spindle assembly and orientation.

ANXA1 is required for planar cell divisions and epithelial morphogenesis

How ANXA1 regulates normal mammary epithelial homeostasis and morphogenesis remains unknown. To characterise ANXA1-expressing cells *in vivo*, we first performed immunostaining experiments in mouse adult virgin mammary glands. We reveal that ANXA1 expression is restricted to the luminal epithelial compartment, where $ANXA1^{+}$ cells selectively co-express the luminal marker E-cadherin and not the basal marker keratin (K)14 (Fig 5A).

Immunofluorescence experiments in human healthy breast tissue confirms that ANXA1 is expressed in the luminal compartment, but also reveal ANXA1 expression in a few α-smooth muscle actin (α-SMA)-positive basal cells (Fig S5A). Consistent with our observations in MCF-10A cells, ANXA1 is mostly detected at the cell cortex of both mouse and human mammary epithelial cells (Fig 5A, Fig S5A). Thus, we conclude that ANXA1 is a surface marker enriched in luminal cells of the murine and human mammary epithelia.

Most studies of mitotic spindle orientation in 3D culture are performed in MDCK and Caco-2 cells, which when grown in reconstituted extracellular matrix (ECM) such as Matrigel, form acini characterised by a central lumen surrounded by a monolayer of polarised epithelial cells [66]. Luminogenesis in MDCK- or Caco-2-derived acini is driven by a tight interplay between planar cell division and apico-basal polarity [67]. Our experiments in MCF-10A-derived acini show that ~60% and ~70% of cells align the mitotic spindle planarly to the basement membrane at 96h and 192h of 3D culture, respectively (Fig S5B and S5C). ANXA1 localises to the cell cortex of mitotic MCF-10A cells (Fig S5D), further indicating that cortical ANXA1 is required for planar mitotic spindle orientation in MCF-10A 3D cultures. However, planar cell divisions do not contribute to cavitation in MCF-10A cell-derived acini (Fig S5B and S5D), consistent with studies showing that a central cavity is formed by apoptosis of inner cells at the end of cystogenesis in this 3D culture system [68]. Remarkably, our experiments in primary human MECs (hMECs) reveal multi-layered acini displaying high architectural heterogeneity (Fig S5E). Out of 601 acini, only 15 (~2.5%) form a central lumen and establish an apico-basal polarity with ANXA1 distributing at the cell cortex and Par6 accumulating at the apical surface (Fig S5E and S5F), suggesting that hMEC are not suitable to study the contribution of OCDs to luminogenesis in 3D culture. Mouse MECs (mMECs) grown in 3D culture self-organise and polarise around a central lumen, which is formed in an apoptosis-independent manner [69, 70]. Therefore, we explored the contribution of ANXA1-mediated regulation of mitotic spindle orientation to luminogenesis in mMEC-derived acini. We isolated MECs from mouse mammary glands at days 15.5-16.5 of pregnancy (P15.5-P16.5) and cultured them in Matrigel [69]. Using immunofluorescence and confocal imaging we first characterised mMECs division modes

throughout epithelial morphogenesis (Fig 5B-5D). After 48h of culture, ~64% of mMECs align their mitotic spindle planar to the basement membrane (angle α 0°-30°), whereas the proportion of mMECs displaying planar divisions increases to ~90% and ~89% at 72h and 96h, respectively (Fig 5B and 5C). This increase in planar divisions is accompanied with a re-organisation of mMECs into a monolayer around an expanding single central lumen that matures at 120h, where mMECs cease to divide and complete their apico-basal polarisation, as revealed by the accumulation of F-actin and Par6 at their apical surface (Fig 5B). Consistent with our results in 2D cultures of MCF-10A cells, ANXA1 distributes at the cell cortex during mitosis in mMECs (Fig 5D). Together these findings, allow us to establish mMEC-derived acini as a unique 3D culture model for the study of the mechanisms linking mitotic spindle orientation to luminogenesis in the mammary epithelium.

To investigate the effect of ANXA1 knockdown on mitotic spindle orientation and luminogenesis in 3D culture, we generated mMECs expressing control or ANXA1 short hairpin (sh) RNAs (sh-Control *versus* sh-ANXA1#1 or sh-ANXA1#2) (Fig 5E). As expected, ~87% of control MECs display planar cell divisions in 72h acini (Fig 5F and 5G). In sharp contrast, ~69% and ~70% of ANXA1-depleted mMECs fail to align planar mitotic spindles, upon sh-ANA1#1 or sh-ANXA1#2 treatment, respectively, with spindle angles α greater than 30° (Fig. 5f, g). Moreover, while LGN localises at the lateral cortex in control mitotic mMECs, ANXA1 depletion impairs its polarised cortical distribution (Fig 5H). By 120h of 3D culture, control acini are mono-layered with a single central lumen, whereas ANXA1-depleted mMECs form larger, disorganised, and multi-layered acini, with multiple small or collapsed lumen (Fig 5I-5K). While controls are circular, ANXA1-depleted acini display irregular and elongated shapes, further indicating aberrant epithelial architecture (Fig 5I and 5J). Our experiments suggest that mitotic spindle misorientation upon ANXA1 knockdown results in daughter cells generated perpendicularly to the epithelial plane, thereby leading to epithelial cell multi-layering, impaired epithelial integrity and luminal collapse. Consistent with this, ANXA1-depleted mMECs display dramatic cytoarchitectural defects and fail to acquire correct apico-basal polarity as revealed by misslocalised E-cadherin and F-actin (Fig 5I and 5L). Thus, ANXA1-mediated regulation of

planar mitotic spindle orientation in mMECs ensures single luminogenesis and normal epithelial morphogenesis.

Discussion

OCDs are essential for establishing proper epithelial tissue architecture and function [3, 4]. Our molecular knowledge of the mechanisms that align the mitotic spindle in polarised epithelia has advanced, largely from extensive studies in model systems in the genetically tractable *Drosophila melanogaster* and *Caenorhabditis elegans* [3, 4]. The $G_{\alpha i}$-LGN-NuMA ternary complex is established as an evolutionarily conserved spindle orientation machinery that anchors the Dynein-Dynactin force generator complex and astral microtubules to the cell cortex, ensuring correct cell division orientation to achieve proper tissue morphogenesis and differentiation [3, 4]. However, the molecular mechanisms governing mitotic spindle positioning in mammalian epithelia remain poorly defined. The present experiments uncover ANXA1, a membrane-associated protein, as a novel interactor of LGN, regulating planar mitotic spindle orientation for correct mammary epithelial morphogenesis. We further report that ANXA1 is an upstream cortical cue that regulates F-actin organisation and instructs LGN and NuMA polarised accumulation at the lateral cortex, ensuring balanced Dynein-Dynactin-mediated pulling forces on astral microtubules and correct alignment of the mitotic spindle (Fig 6).

Cumulative evidence points to additional molecular mechanisms in mammalian cells that control the cortical localisation of LGN upon its $G_{\alpha i}$-mediated active recruitment. A chromosome-derived RANGTP gradient acts in concert with PLK1 to mediate the exclusion of LGN from the cortical regions above chromosomes towards the lateral cortex in HeLa cells [6, 52, 53], where the polarity proteins ABL1 and SAPCD2 also control the cortical abundance of LGN [6, 17, 18, 52]. By contrast, Afadin and E-cadherin facilitate LGN and NuMA recruitment to the lateral cortex in HeLa cells [13] and to the cell-cell contacts in MDCK cells [15], respectively. Our studies in mitotic MCF-10A cells identify ANXA1 as the first-described polarity cue that co-purifies with LGN and controls its dynamic cortical distribution by ensuring its exclusion from the central cortex during prometaphase and stable accumulation at the lateral cortex at metaphase, in a $G_{\alpha i}$-independent manner, thereby directing planar spindle orientation. By comparison, SAPCD2 interacts with LGN to modulate its translocation between the lateral and apical cortical domains to control the balance between planar and perpendicular

divisions, respectively [18]. Upon ANXA1 depletion or inhibition both LGN and NuMA remain at the cell cortex where their restricted lateral accumulation is similarly impaired, suggesting that ANXA1 does not act on the assembly of the LGN-NuMA complex, but rather controls its polarised cortical distribution. This is in sharp contrast with depletion of SAPCD2, Afadin or E-cadherin that abrogates NuMA cortical localisation, where NuMA was shown to compete LGN from SAPCD2, Afadin or E-cadherin [13, 15, 18]. Moreover, our proteomic data show that NuMA co-purifies with the ANXA1-LGN complex, suggesting that ANXA1, LGN and NuMA are likely to form a ternary complex. Structure-function studies will be key to dissect the mechanisms underlying the assembly and spatiotemporal dynamics of the ANXA1-LGN-NuMA complex at the cell cortex and understand how ANXA1 acts with NuMA and synergises with $G_{\alpha i}$ to restrict the cortical accumulation of LGN.

We show that disruption of the polarised cortical localisation of the LGN-NuMA-Dynein-Dynactin complex upon ANXA1 depletion leads to elongated and buckled astral microtubules affecting the assembly and orientation of the mitotic spindle, pointing to a critical role of ANXA1 in the regulation of cortical pulling forces on astral microtubules that control the dynamics of the mitotic spindle. Consistent with this, recent studies have shown that correct cortical targeting of NuMA and its binding to LGN and astral microtubules are required for the dynamic crosstalk between microtubules and the cell cortex and for the stabilisation of Dynein on astral microtubules to generate balanced forces that orient the mitotic spindle [13, 34, 71]. Moreover, ANXA1 depletion impairs F-actin integrity, further suggesting that the protein may regulate the microtubule-actin crosstalk at the cell cortex, which is essential to maintain the balanced forces on astral microtubules that define the mitotic spindle orientation axis [72]. Remarkably, while ANXA1 knockdown affects F-actin organisation and the polarised cortical accumulation of LGN and NuMA, depolymerisation of F-actin using latrunculin A abrogates the recruitment of LGN-NuMA to the cell cortex, similar to what was shown in HeLa cells [13], but has no effect on the localisation of ANXA1 to the plasma membrane. This further reinforces a model whereby ANXA1 acts as an upstream polarity cue that controls the cortical distribution of LGN-NuMA, independently of F-actin. Nonetheless, our results suggest that ANXA1 may also act directly

on F-actin to regulate the microtubule-actin crosstalk at the cell cortex. In fact, ANXA1 has been shown to bind and bundle F-actin in a Ca^{2+}-dependent manner [73]. ANXA1 Ca^{2+}-dependent translocation to the plasma membrane regulates membrane and F-actin dynamics [54, 55]. Furthermore, ANXA1 influences actin dynamics via a direct interaction with the actin polymerising profilin [74, 75]. Additionally, ANXA1 interacts with vimentin, a key F-actin-binding protein that regulates cortical actin organisation and mechanics to ensure normal mitotic progression [63, 76, 77]. Afadin has been shown to bind directly and concomitantly to F-actin and LGN, providing a molecular link between the cell cortex and astral microtubules [13]. Uncovering the molecular mechanisms linking ANXA1 to LGN and F-actin will be key to understand how ANXA1 regulates the astral microtubule-cortical actin crosstalk to ensure balanced pulling forces that orient the mitotic spindle to its correct position.

Defects in LGN-NuMA cortical localisation and spindle orientation can be caused by incorrect metaphase plate formation and chromosome misalignment [52, 53]. Our live imaging experiments reveal that ANXA1 depletion leads to incorrect chromosome segregation and delay in mitotic progression, raising the question of whether the errors that we observe in chromosome segregation are independent of defects in mitotic spindle orientation. Increasing evidence supports that unbalanced astral microtubule-cortex crosstalk leads to defective chromosome dynamics [4, 64]. Additionally, epithelial cell geometry and polarity have been shown to influence chromosome segregation fidelity [78]. Our cortical LGN interactome data identify several NuMA-interacting proteins that have been described to play pleotropic roles in the regulation of astral microtubule stability, mitotic spindle positioning, and kinetochore-microtubule dynamics, including the DYNC1H1/Dynein-p150^{Glued}/Dynactin complex [6, 32-36, 79], CLASP1 [37-39], HAUS6 [40, 41], KPNA2/Importin-α [80], PLK1 [6, 31], TUBG1/γ-tubulin [41, 42], EIF3E/Int-6 [47], CCNB/CDK1 [36, 43], RAN [39, 44, 45]. These findings reinforce the idea that defects in astral microtubule organisation and spindle orientation upon ANXA1 depletion are likely to cause incorrect chromosome segregation. It will be interesting to explore further the molecular mechanisms linking ANXA1-mediated regulation of astral microtubule dynamics to accurate chromosome segregation.

Regulation of the LGN-NuMA complex is essential to maintain the balance between planar and perpendicular divisions that ensures proper position and fate of daughter cells during epithelial morphogenesis and differentiation [3, 4]. Our data in 3D cultures of mMECs demonstrate that ANXA1-mediated control of LGN cortico-lateral localisation and planar spindle orientation is pivotal for normal luminogenesis and epithelial architecture. This is consistent with studies in MDCK, Caco-2 and hepatocytic HepG2 cells establishing LGN as a key regulator of planar cell division during cystogenesis [11, 13, 62, 81, 82]. We establish, for the first time, mMEC-derived acini as a useful 3D culture system to study the mechanisms linking planar spindle orientation to luminogenesis in the mammary epithelium. Our results showing that planar divisions do not contribute to cavitation in MCF-10A cells acini further corroborate previous studies establishing apoptosis as the mechanism that drives cavitation [68]. S1 mammary cells have been used to study the mechanisms of mitotic spindle orientation in 3D culture [83, 84]. However, while S1 cells can form a mature apical membrane, their derived acini do not expand a lumen [85]. During MDCK 3D cystogenesis, early maturation of the apical membrane at the two-cell stage is required for the coupling of apical polarity to mitotic spindle orientation, and aPKC-dependent exclusion of LGN to the lateral cortex, ensuring planar cell division and luminogenesis [11, 67]. Our experiments in mMEC acini suggest, however, that LGN lateral accumulation does not need a mature apical membrane, further sustaining our model establishing ANXA1 as a key polarity cue that instructs LGN restriction to the lateral cortex. Moreover, our data showing that apical polarity is established at d5 of 3D culture after cells have ceased to divide strongly suggest that luminogenesis is driven by planar cell divisions, independently of apical polarity. Interestingly, our proteomic data identify another established LGN-interacting complex, including the LGN adapter INSC and the apical polarity protein PAR3 [3]. While these proteins are essential regulators of the apical localisation of LGN and asymmetric/perpendicular cell division in the mouse skin epidermis and neuroepithelium[3, 4], a study in the mammary gland has shown that mInsc promotes symmetric/planar cell divisions [25], pointing to a context-dependent action of the mechanisms that regulate the localisation and function of the LGN-NuMA to adequately

position cell fate determinants and daughter cells during symmetric/planar or asymmetric/perpendicular cell divisions. Given evidence showing that INSC competes NuMA from LGN [86], it will be interesting to investigate how ANXA1 regulates the interplay between LGN-NuMA and INSC-PAR3 and determine how this influences the switch between perpendicular and planar divisions in the differentiating mammary epithelium.

Our immunofluorescence analysis in hMEC acini show that while ANXA1 localises at the cell cortex, the protein is expressed in both polarised and non-polarised cells that comprise heterogeneous multi-layered acini, which rarely form a central lumen. The inherent morphological heterogeneity observed in hMEC 3D models that we and another study report [87], poses a challenge to the visualisation of OCDs and the characterisation of their relative contribution to human mammary epithelial morphogenesis. Novel culture methods will be needed to assess the functional requirement of ANXA1 in mitotic spindle orientation during hMEC cystogenesis. Our *in situ* experiments reveal that ANXA1 marks a subset of luminal cells in the mouse mammary gland, whereas in human the protein is expressed in both the luminal and basal compartments, further reflecting the intrinsic cellular differences between the mouse and human mammary epithelia. Commonly used mouse cellular lineage markers, such as K5 and K14, have already been described as bimodal in the human breast [88]. Further studies will be necessary to determine whether ANXA1 has distinct or additional functions in the human mammary epithelium from those that we here characterise in mouse.

The balance between symmetric and asymmetric division is broken in breast cancer [3, 24, 26, 27, 89]. Yet, it remains unknown how incorrect mitotic spindle orientation can initiate breast tumorigenesis. Studies in the normal prostate epithelium have shown that depletion of E-cadherin affects the localisation of the LGN-NuMA complex and randomises mitotic spindle orientation, resulting in prostatic hyperplasia that progresses to invasive adenocarcinoma [14]. Thus, defects in OCDs can be envisioned as a key initiating oncogenic event. Our 3D culture experiments show that depletion of ANXA1 leads to epithelial multi-layering, resulting in aberrant epithelial architecture and multiple off-centred small or collapsed lumens, reminiscent of the cribriform growth pattern that is often observed in breast ductal carcinoma *in situ* (DCIS)

[90]. Indeed, cell division-driven epithelial multi-layering where cells escape from the epithelial sheet has been proposed to represent one of the early steps in tumorigenesis [91]. ANXA1 is well established as a biomarker of breast cancer [92] [28]. While the underlying mechanisms remain poorly understood, studies have shown that ANXA1 is downregulated in DCIS whereas it is upregulated in the most aggressive and metastatic breast cancer subtypes [28]. It will be particularly interesting to investigate the functional requirement of ANXA1-mediated mitotic spindle orientation for proper mammary epithelial integrity and differentiation *in vivo*. In parallel, it will also be highly informative to learn more about the fate and dynamics of ANXA1-expressing cells and their relative contributions to mammary gland development and homeostasis, but also to tumour formation and heterogeneity.

Materials and Methods

Cell lines and transfections

MCF-10A, a spontaneously immortalised, nontransformed human mammary epithelial cell (MEC) line (ATCC®) was cultured in DMEM/F12 (Invitrogen) supplemented with 5% donor horse serum (Gibco), 20 ng/ml EGF (Sigma #E9644), 10 µg/ml insulin (Sigma #I1882), 1 ng/ml cholera toxin (Sigma #C8052), 100 µg/ml hydrocortisone (Sigma #H0888), 50 U/ml penicillin, and 50 µg/ml streptomycin (Life Technologies), at 37°C in a humidified 5% CO_2 atmosphere. Cells were transfected with a final concentration of 50 nM si-RNAs using Lipofectamine RNAiMAX (Invitrogen), according to the manufacturer's protocol. Cells were lysed or fixed and immunoprocessed 72h after transfection.

HEK293 cells provided by Melissa Andrews (University of Southampton), were cultured in DMEM supplemented with 10% FBS (Gibco), 50 U/ml penicillin, and 50 µg/ml streptomycin (Life Technologies), at 37°C in a humidified 5% CO_2 atmosphere. Cells were transfected using standard calcium phosphate transfection protocol [93].

Primary mammary epithelial cell 3D culture

Mouse primary MECs (mMECs) were collected from wild-type C57Bl/6 15.5- and 16.5-day pregnant mice and cultured as described [69]. Cells (2×10^4) were plated in each well of 8-well LabTekII chamber slides (Fisher Scientific) pre-coated with Phenol-free Growth Factor Reduced 100% Matrigel (25 µl per well, BD Biosciences) and cultured in DMEM-F12 supplemented with 2% Matrigel, 10% FBS (Gibco), 3 ng/ml EGF (PeproTech #315-09), 1% Glutamine (Sigma), 1 µg/ml Hydrocortisone (Sigma), 10 µg/ml Insulin (Sigma) and 1% Penicillin/Streptomycin (Life Technologies). Cells were grown onto Matrigel to form acini for 2-5 days and fed every 2 days. All animal experiments were performed in accordance with Home Office (UK) regulations and approved by the University of Southampton Local Ethical Committee.

Human MECs (hMECs) were obtained from cryopreserved breast tissue fragments derived from mammary reduction surgeries from healthy donors under informed consent at Mediclinic

(Belgium) as described [94], thawed at 37°C and washed with DMEM-F12 supplemented with antibiotics. After centrifugation at 1500 x rpm for 5 min using DMEM-F12, breast fragments were sheared into smaller fragments using pre-warmed 0.15% Trypsin incubation for 10-15 min at 37°C. hMEC 3D acini were resuspended in 10 mg/ml Cultrex Reduced Growth Factor Basement Membrane Extract (BME) Type 2 (R&D Systems, #3532-005-02) and 25 µl BME domes were plated in each well of µ-Slides 8 (Ibidi). Culture tissue plates were incubated upside down and allowed to polymerise for 30 min at 37°C. 200 µl of hMECs 3D culture medium (Mammary Epithelial Cell Media, Promocell) supplemented with 0.5% FBS, 3 µM Y-27632 (Sigma, #Y0503), Forskolin (Sigma, #F6886), 10 ng/ml Heregulin-β-1 (Peprotech, #100-03) and 10 ng/ml Amphiregulin (Peprotech, #100-55B) were added to each well. Y-27632 and FBS were removed from culture medium after 5 days of culture. Culture medium was refreshed every 3-4 days.

Constructs, siRNAs and shRNAs

Retroviral plasmids were used to transduce MCF-10A cells. pTK14-GFP-LGN plasmid was obtained from Addgene (Plasmid #37360). pTK-GFP was cloned as follows: The full-length eGFP sequence from pTK14 plasmid was amplified by PCR and inserted into the pTK14 plasmid, where the GFP-LGN sequence was removed by restriction digestion with Bsu36i and PspOMI (New England Biolabs). The primers were 5'-CCGACCTGAGGAAGGGAG3-3' (forward) and 5'-ACAGCGGGGCCCTTACTTGTACAGCTCGTCCATGCC-3' (reverse). To clone pTK-ANXA1-mCherry, the ANXA1-mCherry sequence was synthesised (Eurofins) and inserted into pTK93-Lifeact-mCherry vector (Addgene, Plasmid #46357) where Lifeact-mCherry was removed by restriction digestion with NaeI and ApaI (New England Biolabs). pTK-mCherry was cloned as follows: The full-length mCherry sequence was amplified by PCR and inserted into pTK93-Lifeact-mCherry vector where the Lifeact-mCherry sequence was removed by restriction digestion with BamHI and SalI (New England Biolabs). The primers were 5'-AATTGGATCCGCCACCATGGTGAGCAAGGGCGAG-3' (forward) and 5'-

CTGACACACATTCCACAGGGTCG-3' (reverse). For all plasmids, correct insertions were verified by Sanger sequencing.

Transient knockdown of human ANXA1 or LGN in MCF-10A cells was achieved by transfection of MISSION® Predesigned siRNAs from Sigma. The following products were used: SASI_Hs01_00157996 (si-ANXA1#1), SASI_Hs01_00157997 (si-ANXA1#2) for ANXA1 knockdown; SASI_HS01_00121831 (si-LGN#1), SASI_HS01_00121832 (si-LGN#2) for LGN knockdown. siGENOME RISC-Free® (Dharmacon) was used as a negative control (si-Control).

Stable knockdown of mouse ANXA1 in mMECs was performed by small-hairpin RNAs (sh-RNAs). shRNA sequences were annealed and cloned into the pLKO.4-Mem-Venus lentiviral vector, provided by David Bryant (CRUK Beatson Institute University of Glasgow). The following sh-RNA sequences were used: 5'-CCGGGCTTTGGCAGATAAGTCTAATCTCGAGATTAGACTTATCTGCCAAAGCTTTTTG-3' (sh-ANXA1#1 forward) and 5'-CCGGCCGTTCGGAAATTGACATGAACTCGAGTTCATGTCAATTTCCGAACGGTTTTTG-3' (sh-ANXA1#1 reverse); 5'-AATTCAAAAAGCTTTGGCAGATAAGTCTAATCTCGAGATTAGACTTATCTGCCAAAGC-3' (sh-ANXA1#2 forward) and 5'-AATTCAAAAACCGTTCGGAAATTGACATGAACTCGAGTTCATGTCAATTTCCGAACGG-3' (sh-ANXA1#2 reverse). As a negative control, the following sequences were used: 5'-CCGGCCTAAGGTTAAGTCGCCCTCGCTCGAGCGAGGGCGACTTAACCTTAGGTTTTTG-3' (sh-Control forward) and 5'-AATTCAAAAACCTAAGGTTAAGTCGCCCTCGCTCGAGCGAGGGCGACTTAACCTTAGG-3' (sh-Control reverse).

Lentivirus and retrovirus production and infection

To generate stable MCF-10A cell lines, plasmids were introduced by retroviral transduction. Retroviruses were prepared in HEK293 cells by calcium phosphate co-transfection of 10 µg

retroviral plasmid, 6.5 µg envelope plasmid pCMV-VSV-G (Addgene, Plasmid #8454) and 5 µg packaging plasmid pUMVC (Addgene, Plasmid #8449). Virus particles were collected 48 h after transfection, filtered (45 µm) and used to infect MCF-10A cells in the presence of 8 µg/ml polybrene (Sigma). Clones of interest were selected using 2 µg/ml blasticidin (Sigma) or 1 µg/ml puromycin (Sigma). To further enrich for positive cells, selected cells were subjected to flow-cytometry to sort for fluorescent-positive cells.

Knockdown of ANXA1 in mMECs was achieved by lentiviral transduction. Lentiviruses were generated similarly to retrovirus production by co-transfecting 10 µg lentiviral plasmid, 10 µg envelope plasmid pCMV-VSV-G and 10 µg packaging plasmid (pPAX2). pPAX2 plasmid was provided by David Bryant (CRUK Beatson Institute, University of Glasgow). Freshly isolated mMECs were transduced as described [95], and cultured in 8-well slide chambers pre-coated with Matrigel to form acini until immunoprocessing.

Drug treatment

Drugs were dissolved in DMSO and kept at -20°C as 2 mM or 10 mM stock solutions. To synchronise MCF-10A cells in G2/M phase, cells were treated with 9 µM RO-3306 (Sigma #SML0569) for 18h to allow CDK1 inhibition. To further arrest cells in metaphase, MCF-10A cells were released from the G2/M block by washing three times with prewarmed drug-free medium and immediately treated with 10 µM proteasome inhibitor MG-132 (Sigma #474787) for 6h. Cells were washed twice with PBS before processing for experiments. To inhibit TRPM7 kinase activity, MCF-10A cells were treated with 20 µM TG100-115 (Stratech #A2754) for 2h before immunofluorescence. To depolymerise F-actin, cells were treated with 1 µM latrunculin A (Sigma #L5163) for 30 min before immunofluorescence.

Cell extracts and immunoblotting

MCF-10A cells and mMEC 3D acini were lysed in NP-40 buffer [50 mM Tris, pH 7.4, 250 mM NaCl, 5 mM EDTA, 50 mM NaF, 1 mM Na3VO4, 1% Nonidet P40 (NP40)], supplemented with protease inhibitor cocktail (Sigma, #P2714). MEC acini were first treated with trypsin 0.25%

for 30 min to break the Matrigel, then washed with PBS1X and resuspended in NP40 lysis buffer, containing protease inhibitor cocktail, and centrifuged at 14,800 x rpm for 10 min at 4°C. Protein concentration of lysates was determined using Pierce™ BCA Protein Assay (ThermoScientifc) and protein were subjected to SDS-PAGE and subsequent Western blot analysis. The following primary antibodies were used: anti-α-tubulin DM1A (0.2 μg / ml, Sigma #T6199), anti-LGN (1:500, Sigma #ABT174), anti-GFP (2 μg / ml, Invitrogen #A-11122), anti-phospho-Histone3 (0.2 μg / ml, Sigma #06-570), anti-ANXA1 (0.6 μg / ml, Proteintech, #55018-1-AP), anti-mCherry (1:1000, Abcam #ab167453). Secondary antibodies conjugated to horseradish peroxidase (Invitrogen, #32430, #32460) were used at 1:10,000. Protein bands were visualised using SuperSignal™ West Femto Substrate (Thermo Scientific) on a Syngene PXi detection system (Syngene).

Immunoprecipitation and sample preparation for mass spectrometry

MCF-10A cells were plated in 15 cm dishes and washed twice with ice-cold PBS before protein extraction. About 10 x 10^7 cells were lysed in a mild lysis buffer [50 mM Tris, pH 7.4, 150 mM NaCl, 0.5 mM EDTA, 10 mM NaF, 1 mM Na3VO4, 0.5% Nonidet P40 (NP40)], containing protease inhibitor cocktail. Cell lysates were cleared by centrifugation at 17,000x g for 30 min at 4°C. Co-immunoprecipitation was performed using a GFP- or RFP-Trap Kit (Chromotek, #gtma-20, #rtma-20) as per manufacturer's instructions. For immunoblotting, washed beads were eluted by boiling in Laemmli sample buffer (Bio-Rad) containing 5% 2-mercaptoethanol. For mass spectrometry analysis, washed beads were eluted by on-bead tryptic digestion as described [96, 97]. Briefly, proteins on the beads were partially denatured with a buffer containing 2 M urea in 50 mM Tris, pH 7.5, 1 mM DTT. Beads were further treated with a buffer containing 2 M urea in 50 mM Tris, pH 7.5, 5 mM iodoacetamide (IAA) and proteins were eluted by digestion with 5 µg/ml trypsin (Promega). Eluted proteins were fully digested overnight. C18 reverse phase clean-up was performed on the tryptic peptides using a Waters Oasis C18 plate (Waters, UK).

Mass spectrometry and data analysis

Peptide extracts were separated on an Ultimate 3000 RSLC nano system (Thermo Scientific) using a PepMap C18 EASY-Spray LC column, 2 µm particle size, 75 µm x 75 cm column (Thermo Scientific) over a 140 min (single run) linear gradient of 3–25% buffer B (0.1% formic acid in acetonitrile (v/v)) in buffer A (0.1% formic acid in water (v/v)) at a flow rate of 300 nL/min. Peptides were introduced using an EASY-Spray source at 2000 V to a Fusion Tribrid Orbitrap mass spectrometer (Thermo Scientific). Full MS spectra were recorded from 300 to 1500 *m/z* in the Orbitrap at 120,000 resolution with an automatic was performed using TopSpeed mode at a cycle time of 3 s. Higher-energy collisional dissociation (HCD) fragmentation was induced at an energy setting of 28 for peptides with a charge state of 2–4. Fragments were analysed in the orbitrap at 30,000 resolution. Analysis of raw data was performed using Proteome Discoverer software (Thermo Scientific) and the data processed to generate reduced charge state and deisotoped precursor and associated product ion peak lists. These peak lists were searched against the human Uniprot KB database protein database (42,186 entries, 2018-05-18). A maximum of one missed cleavage was allowed for tryptic digestion and the variable modification was set to contain oxidation of methionine and N-terminal protein acetylation. Carboxyamidomethylation of cysteine was set as a fixed modification. The false discovery rate (FDR) was estimated with randomised decoy database searches and were filtered to 1% FDR. Proteins present in the control were removed and further contaminants were also removed by searching against the Contaminant Repository of Affinity Purification (CRAPome) database [30]. The interactions network was constructed with the online STRING protein-protein interaction (PPI) database (v. 11) [98] using an interaction confidence score of ≥ 0.6. The PPI networks were visualised and analysed using Cytoscape software (version 3.8.2) [99]. Gene enrichment analyses were performed to identify Gene Ontology (GO) biological process as well as Reactome and KEGG (Kyoto Encyclopedia of Genes and Genomes) pathways associated with the PPI networks using ClueGO plugin of Cytoscape (version 2.5.7) [100].

Immunofluorescence

The following primary antibodies were used: anti-LGN (1:200, Sigma #ABT174), anti-NuMA (1:100, Novus Biologicals #NB500-174), anti-p150^{Glued} (2.5 μg/ml, BD Biosciences #610473), anti-γ-tubulin AK-15 (1:300, Sigma #T3320), anti-$G_{\alpha i}1$ (10 μg/ml, Santa Cruz #sc-56536), anti-ANXA1 (10 μg/ml, Proteintech #66344-1-Ig; 3 μg/ml, Proteintech #21990-1-AP), anti-S100A11 (10 μg/ml, Proteintech #60024-1-Ig), anti-α-tubulin DM1A (1 μg/ml, Sigma #T6199), anti-E-cadherin (20 μg/ml, Invitrogen #13-1900), anti-Par6 (1 μg/ml, Santa-Cruz #sc-166405), anti-α-Smooth muscle actin (α-SMA) (10 μg/ml, Sigma #A5528), anti-keratin 8 (K8) (5 μg/ml, Sigma #MABT329), anti-K14 (1:300, Origene #BP5009) and anti-GFP (6 μg/ml, Sigma #11814460001). AlexaFluor555 phalloidin (1:100, Life Technologies #A34055) was used to label F-actin. Secondary antibodies (Life Technologies) used were goat anti-mouse (#A-32723), anti-rabbit (#A-11037 and #A-11008), anti-rat (#A-11007) and anti-guineapig (#A-21450) conjugated to AlexaFluor488, AlexaFluor594 or AlexaFluor647, at 5 μg/ml.

To visualise LGN, NuMA, p150^{Glued}, ANXA1, GFP and γ-tubulin, MCF-10A cells were fixed with anhydrous methanol at -20°C for 10 min followed by permeabilisation with 0.1% Triton X-100 in PBS for 2 min. Alternatively, cells were fixed with 10% trichloroacetic acid (TCA, Sigma #T6399) for 7 min on ice followed with anhydrous methanol at -20°C for 10 min. Cells were washed three times before permeabilisation with 0.1% Triton X-100 in PBS for 2 min. $G_{\alpha i1}$ and α-tubulin were visualised by fixing cells with 4% paraformaldehyde (PFA) for 20 min at RT followed by permeabilisation with 0.5% Triton X-100-PBS for 10 min. For all fixation methods, cells were blocked with 3% BSA in 0.1% Triton X-100 in PBS for 1h at RT and immunostained with primary antibodies overnight at 4°C. Cells were washed and incubated with appropriate secondary antibodies for 1h at RT.

To visualise astral microtubules, MCF-10A cells were fixed with 3 % PFA, containing 0.25% glutaraldehyde and 0.2% NP-40 in Brinkley buffer 1980 [(BRB80) 80 mM PIPES, 1 mM MgCl2 hexahydrate, 1 mM EGTA] for 1 min, followed by incubation with 3% PFA and 0.25% glutaraldehyde in BRB80 for 10 min and with 0.1 M NH_4Cl in BRB80 for 10 min. Cells were

washed twice for 5 min with BRB80, permeabilised with 0.5% Triton X-100 in PBS for 10 min, washed again twice in BRB80 and finally blocked in 3% BSA and 0.2% NP-40 in BRB80 for 1h.

For all MCF-10A cell immunostaining, cells were counterstained with 2.5 µg/ml DAPI (Sigma) and mounted with Vectashield antifade mounting medium (Vector Laboratories).

mMEC-derived acini were fixed with 4% PFA for 30 min and permeabilised with 0.5% Triton X-100 in PBS for 10 min. Acini were blocked with 1 % BSA in PBS and 0.1% Triton X-100 for 2h and then incubated with ANXA1, LGN, α-tubulin, E-cadherin primary antibodies overnight at 4°C. Then, acini were immunostained with mouse, rabbit, and rat AlexaFluor488-, AlexaFluor594- or AlexaFluor647-conjugated secondary antibodies for 2h at RT. Acini with F-actin staining at the apical surface of cells surrounding a single lumen were identified as acini with normal lumens. Cells were counterstained with DAPI-containing Fluoroshield (Sigma).

hMEC-derived acini were fixed at day 10 in 2% PFA for 30 min and washed in 1X PBS three times for 10 min. Permeabilisation was performed with 0.5% Triton-100X in 1X PBS for 1h at RT. Acini were then incubated with 0.5% Triton-blocking buffer (5% FBS and 2% BSA in 1X PBS) for 2h at RT. Next, acini were incubated at RT overnight with ANXA1, K8 and Par6 primary antibodies, following washing and incubation with rabbit, rat and mouse AlexaFluor488-, AlexaFluor555-, AlexaFluor647-conjugated secondary antibodies and DAPI for 2h at RT and mounted with Vectashield antifade mounting medium.

Mouse mammary gland sections (50 µm thick) were cut and air-dried for 30 min, then fixed with 4% PFA for 20 min at RT. Following 45 min permeabilisation with 0.2% Triton X-100 in PBS, slides were blocked for 2 h in 2% BSA, 5% foetal bovine serum (FBS), 0.2% Triton X-100 in PBS. Sections were incubated at 4°C overnight in ANXA1, E-cadherin and K14 primary antibodies, washed and incubated with rabbit, rat and guineapig AlexaFluor488-, AlexaFluor594- and AlexaFluor647-conjugated secondary antibodies for 2h at RT. Sections were counterstained with DAPI-containing Fluoroshield.

Freshly dissected breast tissue pieces derived from mammary reduction surgeries from healthy donors were washed in 1X PBS and fixed at 4°C with 2% PFA for 48h. Next, fixed

breast samples were impregnated with 30% Sucrose solution in 1X PBS for at least 48h and embedded in OCT (VWR, #361603E). 70 µm-thick sections were incubated with 0.5% Triton-blocking buffer (5% FBS and 2% BSA in 1X PBS) for 2h at RT. Sections were incubated at RT overnight with ANXA1, E-cadherin and SMA primary antibodies, following washing and incubation with rabbit, rat and mouse AlexaFluor488-, AlexaFluor555-, AlexaFluor647-conjugated secondary antibodies and DAPI for 2h at RT and mounted with Vectashield antifade mounting medium.

Proximity ligation assay

To detect proximal association of ANXA1 and LGN, the Duolink™ proximity ligation assay (PLA) (Sigma, #DUO92102) was used according to the manufacturer's protocol. Briefly**,** MCF-10A cells expressing GFP-LGN were fixed and stained as described in the standard immunofluorescence protocol above. Samples were incubated with ANXA1 and GFP primary antibodies overnight at 4°C. Negative controls were performed by incubating cells with one of the two primary antibodies only. The positive control was performed by visualising the co-localisation of GFP-LGN and LGN. Cells were incubated with Duolink PLA probes for 2h, washed and incubated with the ligation mixture for 30 min, washed again and incubated with the amplification mixture for 2.5h. Cells were counterstained with DAPI-containing Fluoroshield.

Quantitative confocal microscopy

Immunofluorescence images were captured with an inverted Leica TCS SP8 inverted laser scanning microscope (Leica Microsystems) using x40 oil immersion (40x HC Plan/Apo CS2 1.30 numerical aperture (NA)) and x63 glycerol immersion (63x HC Plan/Apo CS2 1.30 NA) objectives. Z-stacks at 16-bit depth and 2048 × 2048 pixels were collected at 0.2 or 0.3 µm (MCF-10A), 0.5 µm (mMECs) and 1 µm (mammary sections) intervals. Images were processed with Fiji software [101]. Astral microtubule images were denoised using ND-Safir 3 software [102]. hMEC acini and human breast tissue images were collected at 12-bit depth

with 1024 x 1024 pixels per tile and then processed using the LasX 3D visualisation software module (Leica Microsystems), and signal intensities were linearly adjusted for visualisation purposes.

ANXA1, LGN and $G_{\alpha i1}$ profiles at the cell cortex of metaphase cells were measured in Fiji using a custom macro as described [103]. Fluorescence intensity values were reported along the cortex starting (and finishing) from a point facing the metaphase plate. Position 0 and 180 face the chromosome plate (central cortex) and position 90 and 270 face spindle poles (lateral cortex): 180 positions were scanned (every 2°) along the cortex. Profiles of ANXA1 and LGN at the cell cortex of prometaphase cells were measured similarly in Fiji with a custom macro (see Supplementary Information). To account for more elongated cell shapes, a line was drawn along the cell contour using the Freehand tool and the macro fits an ellipse to this contour. Fluorescence intensities were calculated along a 30 pixel-long radial line overlapping the cortex and the maximum intensity was reported. The whole cell contour was scanned at 180 successive positions (every 2°) starting (and finishing) at the ellipse's short axis assuming the metaphase plate will align with the long axis of the ellipse. To compare signals from ANXA1 and LGN in prometaphase and metaphase cells, intensity values were corrected by subtracting background measurements. Average profiles were calculated from individual profiles.

Astral microtubule intensity (α-tubulin signal) was measured in Fiji. Maximum projections of images were generated and the fluorescence intensity of the whole cell (I_{total}) and the spindle ($I_{spindle}$) excluding spindle poles with astral microtubules were measured. Background signal was subtracted, and the relative fluorescence intensity of astral microtubules ($I_{astral,\ rel}$) was calculated as $I_{astral,\ rel} = (I_{total} - I_{spindle})/I_{spindle}$. Length of astral microtubules was measured by drawing a line along the astral microtubule extending towards the cell cortex on both sides of the poles. Similarly, the pole-to-cortex distance was measured by drawing a line towards the closest cell cortex in line with the spindle axis. Ratios were calculated by dividing the longer length or distance by the shorter length or distance.

To measure relative fluorescence intensities at the cell cortex and cytoplasm, a 30-pixel line was drawn across the lateral surface and the cytoplasm using Fiji software. The line scan function of Fiji was used to reveal the relative fluorescence intensity across the line.

Ratio of cortical-to-cytoplasmic F-actin fluorescence intensities was measured in Fiji. Maximum projections of images were generated and the fluorescence intensity of the whole cell (I_{total}) and the cytoplasm ($I_{cytoplasm}$) were measured. Background signal was subtracted, and the cortical-to-cytoplasm fluorescence intensity ratio of F-actin ($I_{cortex}/I_{cytoplasm}$) was calculated as $I_{cortex}/I_{cytoplasm} = (I_{total} - I_{cytoplasm})/I_{cytoplasm}$.

Quantifications of number of lumen and shape descriptors (circularity, area/size, roundness), in mMEC acini were performed using Fiji. Acini and lumen were outlined using the Fiji polygon selection tool, followed by shape descriptors extraction. Fluorescence intensities of E-cadherin and F-actin at the cell cortex were analysed using a semi-automated Fiji macro (Cell-o-Tape) [104]. Cell cortex were manually outlined using the Fiji segmented line tool in the E-cadherin channel, and signal intensities of the cellular perimeter were measured. Using the same perimeter, F-actin intensities were measured for the same cell. Graphic representation of both fluorescence intensities was performed by averaging the intensities of all cells per acinus.

Mitotic spindle orientation was measured using Fiji in metaphase cells stained for γ-tubulin (MCF-10A cells) or α-tubulin (acini). In MCF-10A, the spindle axis was defined by drawing a 30-pixel wide line across both spindle poles and repositioned along the z axis. The spindle axis angle was measured in respect to the substratum using the angle tool. Similarly, the spindle axis angle in acini was measured in respect to the plan of the basement membrane.

Quantitative live cell imaging

For live cell imaging, MCF-10A or GFP-LGN-expressing MCF-10A cells were plated in glass bottom dishes (Nunc). Prior to imaging, cells were incubated in cell culture medium supplemented with 100 ng/ml Hoechst 33342 (Sigma) for 30 min. When mitotic spindles were observed, cells were further incubated in cell culture medium supplemented with 100 nM SiR-

tubulin (Spirochrome #251SC002) for 3h. Cells were imaged at 37°C in CO_2 independent medium (Gibco) using a DeltaVision Elite microscope (GE Healthcare) coupled to a sCMOS max chip area 2048 x 2048 camera (G.E. Healthcare). For each recording, image stacks of 30 to 40 planes at 0.6 µm increments were acquired using a PlanApo 60x/1.42 Oil immersion objective (Olympus) with 2x2 binning. Images were taken at 3 stage positions every 2.5 or 3 min for 3 or 5h. Exposure times were 250 msec and 5% laser power for GFP, 80 msec and 2% laser power for labelled DNA and 80 msec and 2% laser power for labelled microtubules using the DAPI-FITC-mCh-Cy5 filter set. Images were deconvolved using the DeltaVision software SoftWoRx and further processed using Fiji.

Mitotic spindle oscillations were calculated from time-lapse videos of MCF-10A cells labelled with SiR-tubulin and Hoechst 33342. Metaphase spindle angles in the z and xy plane were manually determined for every frame using Fiji. Measurements of the spindle angle axis in the z plane were performed as described above in fixed cells. Spindle angles were reported as positive values unless spindle poles changed direction. In this case, angles were displayed as negative values. Mitotic spindle orientation in the xy plane was measured by drawing a line crossing both spindle poles of the first frame of metaphase. This line was embedded to all the following frames to mark the initial position of the mitotic spindle. In the next frame, another line was overlaid across the poles to define the new spindle axis. The angle between the initial spindle position and the current spindle axis was measured using the angle tool. Spindle movement directions were considered by reporting spindle rotations clockwise as positive angles and reverse movements as negative angles. Spindle angle deviations > 10° between two frames were counted as oscillation events. The oscillation index was determined as the percentage of oscillation events in respect to the total number of frames.

Metaphase plates were tracked using IMARIS software (Bitplane). First, a maximum intensity z-projection was created. The DNA metaphase plates were segmented using the Surface module and the centre of the DNA was marked with a point. The movement of this centre point was then tracked automatically over time starting from the first frame of metaphase to the last before anaphase. Movement tracks in the xy plane were reported. Displacement

length was the length of DNA displacement from starting point. Velocity was calculated by the total track length divided by tracking time (metaphase plate congression time).

Statistical analysis

Most of the experiments were repeated at least three times and the exact *n* is stated in the corresponding figure legend. Statistical significance of the overrepresentation of enriched proteins in biological processes and pathways were analysed with the ClueGO App (version 2.5.7) using hypergeometric test (Fisher's Exact Test) and the Bonferroni step-down correction method for multiple testing. Bar graphs of enrichment analyses were created using R statistical software (version 3.6.3) and RStudio (version 1.2.1335). All other statistical analysis were performed with GraphPad Prism 9.0 software. Multiple groups were tested using analysis of variance (ANOVA) with post hoc Tukey test, and comparisons between two groups were performed using *t*-tests. Data are shown as mean ± standard error of the mean (s.e.m.). $P \leq 0.05$ was considered statistically significant. Asterisks indicate levels of significance (* $P \leq 0.05$; ** $P \leq 0.01$; *** $P \leq 0.001$; **** $P \leq 0.0001$). The experiments were not randomised. The investigators were not blinded to allocation during experiments and outcome assessment.

Acknowledgments

We would like to thank Dr Mark Willett at the Imaging and Microscopy Centre for valuable assistance with fluorescence microscopy; Andrew Crocker for mouse husbandry; Dr Melissa Andrews for providing the HEK293 cell line; Dr David Bryant for providing the pLKO.4-Mem-Venus lentiviral plasmid. We would like to thank Wim De Maerteleire, MD for kindly providing us with human healthy breast material from healthy women undergoing reduction mammoplasty. In addition, we thank Dr Marcin Przewloka for critically reviewing the manuscript. This work was supported by a Wellcome Trust Seed Award in Science (210077/Z/17/Z) and MRC New Investigator Research Grant (MR/R026610/1) awarded to SE. MF was supported by a Gerald Kerkut Trust PhD studentship.

Author contributions

MF designed and performed experiments, analysed, and interpreted the data. FSGH performed the bioinformatic analyses. LM and CLGJS performed immunofluorescence and human 3D culture experiments and analysed the data. EL performed rescue and immunofluorescence experiments. MMH performed immunofluorescence and mouse 3D culture experiments. XM designed custom macros for the quantification of cortical fluorescence intensities. PS performed the LC-MS/MS experiments. SE conceived and designed the project, performed experiments, analysed, and interpreted the data, and wrote the manuscript. All the authors provided intellectual input, edited, and approved the final manuscript.

Supplementary information

Supplementary Information includes 5 figures, two tables, and one Fiji macro.

Competing interests

The authors declare no competing financial interests.

Data availability

All the data that support the findings of this study are available within the paper and its supplementary information files. Further information and requests for all other relevant data and reagents are available from the corresponding author upon reasonable request. The mass spectrometry proteomics data have been deposited the ProteomeXchange Consortium via the PRIDE partner repository [29] with the dataset identifier PXD027452.

References

1. Morin X, Bellaiche Y. Mitotic spindle orientation in asymmetric and symmetric cell divisions during animal development. Dev Cell. 2011;21(1):102-19. Epub 2011/07/19. doi: 10.1016/j.devcel.2011.06.012. PubMed PMID: 21763612.

2. Mukherjee S, Kong J, Brat DJ. Cancer stem cell division: when the rules of asymmetry are broken. Stem Cells Dev. 2015;24(4):405-16. Epub 2014/11/11. doi: 10.1089/scd.2014.0442. PubMed PMID: 25382732; PubMed Central PMCID: PMCPMC4313409.

3. Santoro A, Vlachou T, Carminati M, Pelicci PG, Mapelli M. Molecular mechanisms of asymmetric divisions in mammary stem cells. EMBO Rep. 2016;17(12):1700-20. Epub 2016/11/23. doi: 10.15252/embr.201643021. PubMed PMID: 27872203; PubMed Central PMCID: PMCPMC5283594.

4. di Pietro F, Echard A, Morin X. Regulation of mitotic spindle orientation: an integrated view. EMBO Rep. 2016;17(8):1106-30. Epub 2016/07/20. doi: 10.15252/embr.201642292. PubMed PMID: 27432284; PubMed Central PMCID: PMCPMC4967962.

5. Kiyomitsu T. The cortical force-generating machinery: how cortical spindle-pulling forces are generated. Curr Opin Cell Biol. 2019;60:1-8. Epub 2019/04/08. doi: 10.1016/j.ceb.2019.03.001. PubMed PMID: 30954860.

6. Kiyomitsu T, Cheeseman IM. Chromosome- and spindle-pole-derived signals generate an intrinsic code for spindle position and orientation. Nat Cell Biol. 2012;14(3):311-7. Epub 2012/02/14. doi: 10.1038/ncb2440. PubMed PMID: 22327364; PubMed Central PMCID: PMCPMC3290711.

7. Bergstralh DT, Dawney NS, St Johnston D. Spindle orientation: a question of complex positioning. Development. 2017;144(7):1137-45. Epub 2017/03/30. doi: 10.1242/dev.140764. PubMed PMID: 28351864.

8. Schaefer M, Shevchenko A, Shevchenko A, Knoblich JA. A protein complex containing Inscuteable and the Galpha-binding protein Pins orients asymmetric cell divisions in Drosophila. Curr Biol. 2000;10(7):353-62. Epub 2001/02/07. doi: 10.1016/s0960-9822(00)00401-2. PubMed PMID: 10753746.

9. Yu F, Morin X, Cai Y, Yang X, Chia W. Analysis of partner of inscuteable, a novel player of Drosophila asymmetric divisions, reveals two distinct steps in inscuteable apical localization. Cell. 2000;100(4):399-409. Epub 2000/02/29. doi: 10.1016/s0092-8674(00)80676-5. PubMed PMID: 10693757.

10. Williams SE, Ratliff LA, Postiglione MP, Knoblich JA, Fuchs E. Par3-mInsc and Galphai3 cooperate to promote oriented epidermal cell divisions through LGN. Nat Cell Biol. 2014;16(8):758-69. Epub 2014/07/16. doi: 10.1038/ncb3001. PubMed PMID: 25016959; PubMed Central PMCID: PMCPMC4159251.

11. Hao Y, Du Q, Chen X, Zheng Z, Balsbaugh JL, Maitra S, et al. Par3 controls epithelial spindle orientation by aPKC-mediated phosphorylation of apical Pins. Curr Biol. 2010;20(20):1809-18. Epub 2010/10/12. doi: 10.1016/j.cub.2010.09.032. PubMed PMID: 20933426; PubMed Central PMCID: PMCPMC2963683.

12. Woodard GE, Huang NN, Cho H, Miki T, Tall GG, Kehrl JH. Ric-8A and Gi alpha recruit LGN, NuMA, and dynein to the cell cortex to help orient the mitotic spindle. Mol Cell Biol. 2010;30(14):3519-30. Epub 2010/05/19. doi: 10.1128/MCB.00394-10. PubMed PMID: 20479129; PubMed Central PMCID: PMCPMC2897540.

13. Carminati M, Gallini S, Pirovano L, Alfieri A, Bisi S, Mapelli M. Concomitant binding of Afadin to LGN and F-actin directs planar spindle orientation. Nat Struct Mol Biol. 2016;23(2):155-63. Epub 2016/01/12. doi: 10.1038/nsmb.3152. PubMed PMID: 26751642.

14. Wang X, Dong B, Zhang K, Ji Z, Cheng C, Zhao H, et al. E-cadherin bridges cell polarity and spindle orientation to ensure prostate epithelial integrity and prevent carcinogenesis in vivo. PLoS Genet. 2018;14(8):e1007609. Epub 2018/08/18. doi: 10.1371/journal.pgen.1007609. PubMed PMID: 30118484; PubMed Central PMCID: PMCPMC6115016.

15. Gloerich M, Bianchini JM, Siemers KA, Cohen DJ, Nelson WJ. Cell division orientation is coupled to cell-cell adhesion by the E-cadherin/LGN complex. Nat Commun. 2017;8:13996. Epub 2017/01/04. doi: 10.1038/ncomms13996. PubMed PMID: 28045117; PubMed Central PMCID: PMCPMC5216124.

16. Porter AP, White GRM, Mack NA, Malliri A. The interaction between CASK and the tumour suppressor Dlg1 regulates mitotic spindle orientation in mammalian epithelia. J Cell Sci. 2019;132(14). Epub 2019/07/11. doi: 10.1242/jcs.230086. PubMed PMID: 31289196; PubMed Central PMCID: PMCPMC6679578.

17. Matsumura S, Hamasaki M, Yamamoto T, Ebisuya M, Sato M, Nishida E, et al. ABL1 regulates spindle orientation in adherent cells and mammalian skin. Nat Commun. 2012;3:626. Epub 2012/01/19. doi: 10.1038/ncomms1634. PubMed PMID: 22252550; PubMed Central PMCID: PMCPMC3324324.

18. Chiu CWN, Monat C, Robitaille M, Lacomme M, Daulat AM, Macleod G, et al. SAPCD2 Controls Spindle Orientation and Asymmetric Divisions by Negatively Regulating the Galphai-LGN-NuMA Ternary Complex. Dev Cell. 2016;36(1):50-62. Epub 2016/01/15. doi: 10.1016/j.devcel.2015.12.016. PubMed PMID: 26766442.

19. Fu NY, Nolan E, Lindeman GJ, Visvader JE. Stem Cells and the Differentiation Hierarchy in Mammary Gland Development. Physiol Rev. 2020;100(2):489-523. Epub 2019/09/21. doi: 10.1152/physrev.00040.2018. PubMed PMID: 31539305.

20. Taddei I, Deugnier MA, Faraldo MM, Petit V, Bouvard D, Medina D, et al. Beta1 integrin deletion from the basal compartment of the mammary epithelium affects stem cells. Nat Cell Biol. 2008;10(6):716-22. Epub 2008/05/13. doi: 10.1038/ncb1734. PubMed PMID: 18469806; PubMed Central PMCID: PMCPMC2659707.

21. Regan JL, Sourisseau T, Soady K, Kendrick H, McCarthy A, Tang C, et al. Aurora A kinase regulates mammary epithelial cell fate by determining mitotic spindle orientation in a Notch-dependent manner. Cell Rep. 2013;4(1):110-23. Epub 2013/07/03. doi: 10.1016/j.celrep.2013.05.044. PubMed PMID: 23810554.

22. Elias S, Thion MS, Yu H, Sousa CM, Lasgi C, Morin X, et al. Huntingtin regulates mammary stem cell division and differentiation. Stem Cell Reports. 2014;2(4):491-506. Epub 2014/04/22. doi: 10.1016/j.stemcr.2014.02.011. PubMed PMID: 24749073; PubMed Central PMCID: PMCPMC3986500.

23. Villegas E, Kabotyanski EB, Shore AN, Creighton CJ, Westbrook TF, Rosen JM. Plk2 regulates mitotic spindle orientation and mammary gland development. Development. 2014;141(7):1562-71. Epub 2014/03/07. doi: 10.1242/dev.108258. PubMed PMID: 24598160; PubMed Central PMCID: PMCPMC3957376.

24. Morris EJ, Gillespie JA, Maxwell CA, Dedhar S. A Model of Differential Mammary Growth Initiation by Stat3 and Asymmetric Integrin-alpha6 Inheritance. Cell Rep.

2020;30(11):3605-15 e5. Epub 2020/03/19. doi: 10.1016/j.celrep.2020.02.079. PubMed PMID: 32187533.

25. Ballard MS, Zhu A, Iwai N, Stensrud M, Mapps A, Postiglione MP, et al. Mammary Stem Cell Self-Renewal Is Regulated by Slit2/Robo1 Signaling through SNAI1 and mINSC. Cell Rep. 2015;13(2):290-301. Epub 2015/10/07. doi: 10.1016/j.celrep.2015.09.006. PubMed PMID: 26440891; PubMed Central PMCID: PMCPMC4606466.

26. Segatto I, Zompit MM, Citron F, D'Andrea S, Vinciguerra GLR, Perin T, et al. Stathmin Is Required for Normal Mouse Mammary Gland Development and Delta16HER2-Driven Tumorigenesis. Cancer Res. 2019;79(2):397-409. Epub 2018/11/28. doi: 10.1158/0008-5472.CAN-18-2488. PubMed PMID: 30478213.

27. Santoro A, Vlachou T, Luzi L, Melloni G, Mazzarella L, D'Elia E, et al. p53 Loss in Breast Cancer Leads to Myc Activation, Increased Cell Plasticity, and Expression of a Mitotic Signature with Prognostic Value. Cell Rep. 2019;26(3):624-38 e8. Epub 2019/01/17. doi: 10.1016/j.celrep.2018.12.071. PubMed PMID: 30650356; PubMed Central PMCID: PMCPMC6334229.

28. Foo SL, Yap G, Cui J, Lim LHK. Annexin-A1 - A Blessing or a Curse in Cancer? Trends Mol Med. 2019;25(4):315-27. Epub 2019/03/16. doi: 10.1016/j.molmed.2019.02.004. PubMed PMID: 30871809.

29. Perez-Riverol Y, Csordas A, Bai J, Bernal-Llinares M, Hewapathirana S, Kundu DJ, et al. The PRIDE database and related tools and resources in 2019: improving support for quantification data. Nucleic Acids Res. 2019;47(D1):D442-D50. Epub 2018/11/06. doi: 10.1093/nar/gky1106. PubMed PMID: 30395289; PubMed Central PMCID: PMCPMC6323896.

30. Mellacheruvu D, Wright Z, Couzens AL, Lambert JP, St-Denis NA, Li T, et al. The CRAPome: a contaminant repository for affinity purification-mass spectrometry data. Nat Methods. 2013;10(8):730-6. Epub 2013/08/08. doi: 10.1038/nmeth.2557. PubMed PMID: 23921808; PubMed Central PMCID: PMCPMC3773500.

31. Liu XS, Song B, Tang J, Liu W, Kuang S, Liu X. Plk1 phosphorylates Sgt1 at the kinetochores to promote timely kinetochore-microtubule attachment. Mol Cell Biol. 2012;32(19):4053-67. Epub 2012/08/08. doi: 10.1128/MCB.00516-12. PubMed PMID: 22869522; PubMed Central PMCID: PMCPMC3457539.

32. Busson S, Dujardin D, Moreau A, Dompierre J, De Mey JR. Dynein and dynactin are localized to astral microtubules and at cortical sites in mitotic epithelial cells. Curr Biol. 1998;8(9):541-4. Epub 1998/05/20. doi: 10.1016/s0960-9822(98)70208-8. PubMed PMID: 9560347.

33. Zheng Z, Wan Q, Liu J, Zhu H, Chu X, Du Q. Evidence for dynein and astral microtubule-mediated cortical release and transport of Galphai/LGN/NuMA complex in mitotic cells. Mol Biol Cell. 2013;24(7):901-13. Epub 2013/02/08. doi: 10.1091/mbc.E12-06-0458. PubMed PMID: 23389635; PubMed Central PMCID: PMCPMC3608500.

34. Okumura M, Natsume T, Kanemaki MT, Kiyomitsu T. Dynein-Dynactin-NuMA clusters generate cortical spindle-pulling forces as a multi-arm ensemble. Elife. 2018;7. Epub 2018/06/01. doi: 10.7554/eLife.36559. PubMed PMID: 29848445; PubMed Central PMCID: PMCPMC6037482.

35. Yang Z, Tulu US, Wadsworth P, Rieder CL. Kinetochore dynein is required for chromosome motion and congression independent of the spindle checkpoint. Curr Biol.

2007;17(11):973-80. Epub 2007/05/19. doi: 10.1016/j.cub.2007.04.056. PubMed PMID: 17509882; PubMed Central PMCID: PMCPMC2570756.

36. Musacchio A. The Molecular Biology of Spindle Assembly Checkpoint Signaling Dynamics. Curr Biol. 2015;25(20):R1002-18. Epub 2015/10/21. doi: 10.1016/j.cub.2015.08.051. PubMed PMID: 26485365.

37. Maiato H, Rieder CL, Earnshaw WC, Sunkel CE. How do kinetochores CLASP dynamic microtubules? Cell Cycle. 2003;2(6):511-4. Epub 2003/09/25. doi: 10.4161/cc.2.6.576. PubMed PMID: 14504462.

38. Pereira AL, Pereira AJ, Maia AR, Drabek K, Sayas CL, Hergert PJ, et al. Mammalian CLASP1 and CLASP2 cooperate to ensure mitotic fidelity by regulating spindle and kinetochore function. Mol Biol Cell. 2006;17(10):4526-42. Epub 2006/08/18. doi: 10.1091/mbc.e06-07-0579. PubMed PMID: 16914514; PubMed Central PMCID: PMCPMC1635371.

39. Bird SL, Heald R, Weis K. RanGTP and CLASP1 cooperate to position the mitotic spindle. Mol Biol Cell. 2013;24(16):2506-14. Epub 2013/06/21. doi: 10.1091/mbc.E13-03-0150. PubMed PMID: 23783028; PubMed Central PMCID: PMCPMC3744954.

40. David AF, Roudot P, Legant WR, Betzig E, Danuser G, Gerlich DW. Augmin accumulation on long-lived microtubules drives amplification and kinetochore-directed growth. J Cell Biol. 2019;218(7):2150-68. Epub 2019/05/23. doi: 10.1083/jcb.201805044. PubMed PMID: 31113824; PubMed Central PMCID: PMCPMC6605806.

41. Bouissou A, Verollet C, de Forges H, Haren L, Bellaiche Y, Perez F, et al. gamma-Tubulin Ring Complexes and EB1 play antagonistic roles in microtubule dynamics and spindle positioning. EMBO J. 2014;33(2):114-28. Epub 2014/01/15. doi: 10.1002/embj.201385967. PubMed PMID: 24421324; PubMed Central PMCID: PMCPMC3989606.

42. Mishra RK, Chakraborty P, Arnaoutov A, Fontoura BM, Dasso M. The Nup107-160 complex and gamma-TuRC regulate microtubule polymerization at kinetochores. Nat Cell Biol. 2010;12(2):164-9. Epub 2010/01/19. doi: 10.1038/ncb2016. PubMed PMID: 20081840; PubMed Central PMCID: PMCPMC2859955.

43. Singh D, Schmidt N, Muller F, Bange T, Bird AW. Destabilization of Long Astral Microtubules via Cdk1-Dependent Removal of GTSE1 from Their Plus Ends Facilitates Prometaphase Spindle Orientation. Curr Biol. 2021;31(4):766-81 e8. Epub 2020/12/18. doi: 10.1016/j.cub.2020.11.040. PubMed PMID: 33333009.

44. Sillje HH, Nagel S, Korner R, Nigg EA. HURP is a Ran-importin beta-regulated protein that stabilizes kinetochore microtubules in the vicinity of chromosomes. Curr Biol. 2006;16(8):731-42. Epub 2006/04/25. doi: 10.1016/j.cub.2006.02.070. PubMed PMID: 16631580.

45. Wilde A, Zheng Y. Stimulation of microtubule aster formation and spindle assembly by the small GTPase Ran. Science. 1999;284(5418):1359-62. Epub 1999/05/21. doi: 10.1126/science.284.5418.1359. PubMed PMID: 10334991.

46. Grzmil M, Rzymski T, Milani M, Harris AL, Capper RG, Saunders NJ, et al. An oncogenic role of eIF3e/INT6 in human breast cancer. Oncogene. 2010;29(28):4080-9. Epub 2010/05/11. doi: 10.1038/onc.2010.152. PubMed PMID: 20453879.

47. Morris C, Jalinot P. Silencing of human Int-6 impairs mitosis progression and inhibits cyclin B-Cdk1 activation. Oncogene. 2005;24(7):1203-11. Epub 2004/11/24. doi: 10.1038/sj.onc.1208268. PubMed PMID: 15558017.

48. Flower RJ, Blackwell GJ. Anti-inflammatory steroids induce biosynthesis of a phospholipase A2 inhibitor which prevents prostaglandin generation. Nature. 1979;278(5703):456-9. Epub 1979/03/29. doi: 10.1038/278456a0. PubMed PMID: 450050.

49. Watanabe M, Ando Y, Todoroki H, Minami H, Hidaka H. Molecular cloning and sequencing of a cDNA clone encoding a new calcium binding protein, named calgizzarin, from rabbit lung. Biochem Biophys Res Commun. 1991;181(2):644-9. Epub 1991/12/16. doi: 10.1016/0006-291x(91)91239-9. PubMed PMID: 1836726.

50. De Buck M, Gouwy M, Wang JM, Van Snick J, Opdenakker G, Struyf S, et al. Structure and Expression of Different Serum Amyloid A (SAA) Variants and their Concentration-Dependent Functions During Host Insults. Curr Med Chem. 2016;23(17):1725-55. Epub 2016/04/19. doi: 10.2174/0929867323666160418114600. PubMed PMID: 27087246; PubMed Central PMCID: PMCPMC5405626.

51. Perretti M, D'Acquisto F. Annexin A1 and glucocorticoids as effectors of the resolution of inflammation. Nat Rev Immunol. 2009;9(1):62-70. Epub 2008/12/24. doi: 10.1038/nri2470. PubMed PMID: 19104500.

52. Tame MA, Raaijmakers JA, Afanasyev P, Medema RH. Chromosome misalignments induce spindle-positioning defects. EMBO Rep. 2016;17(3):317-25. Epub 2016/02/18. doi: 10.15252/embr.201541143. PubMed PMID: 26882550; PubMed Central PMCID: PMCPMC4772978.

53. Sana S, Keshri R, Rajeevan A, Kapoor S, Kotak S. Plk1 regulates spindle orientation by phosphorylating NuMA in human cells. Life Sci Alliance. 2018;1(6):e201800223. Epub 2018/11/21. doi: 10.26508/lsa.201800223. PubMed PMID: 30456393; PubMed Central PMCID: PMCPMC6240335.

54. Jaiswal JK, Lauritzen SP, Scheffer L, Sakaguchi M, Bunkenborg J, Simon SM, et al. S100A11 is required for efficient plasma membrane repair and survival of invasive cancer cells. Nat Commun. 2014;5:3795. Epub 2014/05/09. doi: 10.1038/ncomms4795. PubMed PMID: 24806074; PubMed Central PMCID: PMCPMC4026250.

55. Rintala-Dempsey AC, Rezvanpour A, Shaw GS. S100-annexin complexes--structural insights. FEBS J. 2008;275(20):4956-66. Epub 2008/09/18. doi: 10.1111/j.1742-4658.2008.06654.x. PubMed PMID: 18795951.

56. Kastl K, Ross M, Gerke V, Steinem C. Kinetics and thermodynamics of annexin A1 binding to solid-supported membranes: a QCM study. Biochemistry. 2002;41(31):10087-94. doi: 10.1021/bi025951z. PubMed PMID: 12146973.

57. Dorovkov MV, Ryazanov AG. Phosphorylation of annexin I by TRPM7 channel-kinase. J Biol Chem. 2004;279(49):50643-6. Epub 2004/10/16. doi: 10.1074/jbc.C400441200. PubMed PMID: 15485879.

58. Song C, Bae Y, Jun J, Lee H, Kim ND, Lee KB, et al. Identification of TG100-115 as a new and potent TRPM7 kinase inhibitor, which suppresses breast cancer cell migration and invasion. Biochim Biophys Acta Gen Subj. 2017;1861(4):947-57. Epub 20170201. doi: 10.1016/j.bbagen.2017.01.034. PubMed PMID: 28161478.

59. Lukinavicius G, Reymond L, D'Este E, Masharina A, Gottfert F, Ta H, et al. Fluorogenic probes for live-cell imaging of the cytoskeleton. Nat Methods. 2014;11(7):731-3. Epub 2014/05/27. doi: 10.1038/nmeth.2972. PubMed PMID: 24859753.

60. Peyre E, Jaouen F, Saadaoui M, Haren L, Merdes A, Durbec P, et al. A lateral belt of cortical LGN and NuMA guides mitotic spindle movements and planar division in neuroepithelial cells. J Cell Biol. 2011;193(1):141-54. Epub 2011/03/30. doi: 10.1083/jcb.201101039. PubMed PMID: 21444683; PubMed Central PMCID: PMCPMC3082188.

61. Williams SE, Beronja S, Pasolli HA, Fuchs E. Asymmetric cell divisions promote Notch-dependent epidermal differentiation. Nature. 2011;470(7334):353-8. Epub 2011/02/19. doi: 10.1038/nature09793. PubMed PMID: 21331036; PubMed Central PMCID: PMCPMC3077085.

62. Zheng Z, Zhu H, Wan Q, Liu J, Xiao Z, Siderovski DP, et al. LGN regulates mitotic spindle orientation during epithelial morphogenesis. J Cell Biol. 2010;189(2):275-88. Epub 2010/04/14. doi: 10.1083/jcb.200910021. PubMed PMID: 20385777; PubMed Central PMCID: PMCPMC2856901.

63. Serres MP, Samwer M, Truong Quang BA, Lavoie G, Perera U, Gorlich D, et al. F-Actin Interactome Reveals Vimentin as a Key Regulator of Actin Organization and Cell Mechanics in Mitosis. Dev Cell. 2020;52(2):210-22 e7. Epub 2020/01/14. doi: 10.1016/j.devcel.2019.12.011. PubMed PMID: 31928973; PubMed Central PMCID: PMCPMC6983945.

64. Yu H, Yang F, Dong P, Liao S, Liu WR, Zhao G, et al. NDP52 tunes cortical actin interaction with astral microtubules for accurate spindle orientation. Cell Res. 2019;29(8):666-79. Epub 2019/06/16. doi: 10.1038/s41422-019-0189-9. PubMed PMID: 31201383; PubMed Central PMCID: PMCPMC6796859.

65. Hayes MJ, Rescher U, Gerke V, Moss SE. Annexin-actin interactions. Traffic. 2004;5(8):571-6. doi: 10.1111/j.1600-0854.2004.00210.x. PubMed PMID: 15260827.

66. Zegers MM, O'Brien LE, Yu W, Datta A, Mostov KE. Epithelial polarity and tubulogenesis in vitro. Trends Cell Biol. 2003;13(4):169-76. doi: 10.1016/s0962-8924(03)00036-9. PubMed PMID: 12667754.

67. Roman-Fernandez A, Bryant DM. Complex Polarity: Building Multicellular Tissues Through Apical Membrane Traffic. Traffic. 2016;17(12):1244-61. Epub 20160701. doi: 10.1111/tra.12417. PubMed PMID: 27281121.

68. Debnath J, Mills KR, Collins NL, Reginato MJ, Muthuswamy SK, Brugge JS. The role of apoptosis in creating and maintaining luminal space within normal and oncogene-expressing mammary acini. Cell. 2002;111(1):29-40. doi: 10.1016/s0092-8674(02)01001-2. PubMed PMID: 12372298.

69. Ahmed MI, Elias S, Mould AW, Bikoff EK, Robertson EJ. The transcriptional repressor Blimp1 is expressed in rare luminal progenitors and is essential for mammary gland development. Development. 2016;143(10):1663-73. Epub 2016/05/18. doi: 10.1242/dev.136358. PubMed PMID: 27190036; PubMed Central PMCID: PMCPMC4874485.

70. Akhtar N, Streuli CH. An integrin-ILK-microtubule network orients cell polarity and lumen formation in glandular epithelium. Nat Cell Biol. 2013;15(1):17-27. Epub 2012/12/25. doi: 10.1038/ncb2646. PubMed PMID: 23263281; PubMed Central PMCID: PMCPMC3701152.

71. Pirovano L, Culurgioni S, Carminati M, Alfieri A, Monzani S, Cecatiello V, et al. Hexameric NuMA:LGN structures promote multivalent interactions required for planar epithelial divisions. Nat Commun. 2019;10(1):2208. Epub 2019/05/19. doi: 10.1038/s41467-019-09999-w. PubMed PMID: 31101817; PubMed Central PMCID: PMCPMC6525239.

72. Dogterom M, Koenderink GH. Actin-microtubule crosstalk in cell biology. Nat Rev Mol Cell Biol. 2019;20(1):38-54. Epub 2018/10/17. doi: 10.1038/s41580-018-0067-1. PubMed PMID: 30323238.

73. Glenney JR, Jr., Tack B, Powell MA. Calpactins: two distinct Ca++-regulated phospholipid- and actin-binding proteins isolated from lung and placenta. J Cell Biol. 1987;104(3):503-11. Epub 1987/03/01. doi: 10.1083/jcb.104.3.503. PubMed PMID: 2950118; PubMed Central PMCID: PMCPMC2114563.

74. Alvarez-Martinez MT, Mani JC, Porte F, Faivre-Sarrailh C, Liautard JP, Sri Widada J. Characterization of the interaction between annexin I and profilin. Eur J Biochem. 1996;238(3):777-84. Epub 1996/06/15. doi: 10.1111/j.1432-1033.1996.0777w.x. PubMed PMID: 8706680.

75. Alvarez-Martinez MT, Porte F, Liautard JP, Sri Widada J. Effects of profilin-annexin I association on some properties of both profilin and annexin I: modification of the inhibitory activity of profilin on actin polymerization and inhibition of the self-association of annexin I and its interactions with liposomes. Biochim Biophys Acta. 1997;1339(2):331-40. Epub 1997/05/23. doi: 10.1016/s0167-4838(97)00018-6. PubMed PMID: 9187254.

76. Xiao Y, Ouyang C, Huang W, Tang Y, Fu W, Cheng A. Annexin A1 can inhibit the in vitro invasive ability of nasopharyngeal carcinoma cells possibly through Annexin A1/S100A9/Vimentin interaction. PLoS One. 2017;12(3):e0174383. Epub 2017/03/30. doi: 10.1371/journal.pone.0174383. PubMed PMID: 28355254; PubMed Central PMCID: PMCPMC5371313.

77. Duarte S, Viedma-Poyatos A, Navarro-Carrasco E, Martinez AE, Pajares MA, Perez-Sala D. Vimentin filaments interact with the actin cortex in mitosis allowing normal cell division. Nat Commun. 2019;10(1):4200. Epub 2019/09/15. doi: 10.1038/s41467-019-12029-4. PubMed PMID: 31519880; PubMed Central PMCID: PMCPMC6744490.

78. Knouse KA, Lopez KE, Bachofner M, Amon A. Chromosome Segregation Fidelity in Epithelia Requires Tissue Architecture. Cell. 2018;175(1):200-11 e13. Epub 2018/08/28. doi: 10.1016/j.cell.2018.07.042. PubMed PMID: 30146160; PubMed Central PMCID: PMCPMC6151153.

79. Howell BJ, McEwen BF, Canman JC, Hoffman DB, Farrar EM, Rieder CL, et al. Cytoplasmic dynein/dynactin drives kinetochore protein transport to the spindle poles and has a role in mitotic spindle checkpoint inactivation. J Cell Biol. 2001;155(7):1159-72. Epub 2002/01/05. doi: 10.1083/jcb.200105093. PubMed PMID: 11756470; PubMed Central PMCID: PMCPMC2199338.

80. Guo H, Wei JH, Zhang Y, Seemann J. Importin alpha phosphorylation promotes TPX2 activation by GM130 to control astral microtubules and spindle orientation. J Cell Sci. 2021;134(4). Epub 2021/02/03. doi: 10.1242/jcs.258356. PubMed PMID: 33526712; PubMed Central PMCID: PMCPMC7904092.

81. Chishiki K, Kamakura S, Hayase J, Sumimoto H. Ric-8A, an activator protein of Galphai, controls mammalian epithelial cell polarity for tight junction assembly and cystogenesis. Genes Cells. 2017;22(3):293-309. Epub 2017/02/12. doi: 10.1111/gtc.12477. PubMed PMID: 28185378.

82. Lazaro-Dieguez F, Cohen D, Fernandez D, Hodgson L, van Ijzendoorn SC, Musch A. Par1b links lumen polarity with LGN-NuMA positioning for distinct epithelial cell division phenotypes. J Cell Biol. 2013;203(2):251-64. Epub 2013/10/30. doi: 10.1083/jcb.201303013. PubMed PMID: 24165937; PubMed Central PMCID: PMCPMC3812971.

83. Bazzoun D, Adissu HA, Wang L, Urazaev A, Tenvooren I, Fostok SF, et al. Connexin 43 maintains tissue polarity and regulates mitotic spindle orientation in the breast epithelium. J Cell Sci. 2019;132(10). Epub 20190516. doi: 10.1242/jcs.223313. PubMed PMID: 30992345; PubMed Central PMCID: PMCPMC6550011.

84. Tenvooren I, Jenks MZ, Rashid H, Cook KL, Muhlemann JK, Sistrunk C, et al. Elevated leptin disrupts epithelial polarity and promotes premalignant alterations in the mammary gland. Oncogene. 2019;38(20):3855-70. Epub 20190122. doi: 10.1038/s41388-019-0687-8. PubMed PMID: 30670780; PubMed Central PMCID: PMCPMC6525037.

85. Plachot C, Chaboub LS, Adissu HA, Wang L, Urazaev A, Sturgis J, et al. Factors necessary to produce basoapical polarity in human glandular epithelium formed in conventional and high-throughput three-dimensional culture: example of the breast epithelium. BMC Biol. 2009;7:77. Epub 20091116. doi: 10.1186/1741-7007-7-77. PubMed PMID: 19917093; PubMed Central PMCID: PMCPMC2784453.

86. Culurgioni S, Alfieri A, Pendolino V, Laddomada F, Mapelli M. Inscuteable and NuMA proteins bind competitively to Leu-Gly-Asn repeat-enriched protein (LGN) during asymmetric cell divisions. Proc Natl Acad Sci U S A. 2011;108(52):20998-1003. Epub 20111214. doi: 10.1073/pnas.1113077108. PubMed PMID: 22171003; PubMed Central PMCID: PMCPMC3248549.

87. Rosenbluth JM, Schackmann RCJ, Gray GK, Selfors LM, Li CM, Boedicker M, et al. Organoid cultures from normal and cancer-prone human breast tissues preserve complex epithelial lineages. Nat Commun. 2020;11(1):1711. Epub 20200406. doi: 10.1038/s41467-020-15548-7. PubMed PMID: 32249764; PubMed Central PMCID: PMCPMC7136203.

88. Santagata S, Thakkar A, Ergonul A, Wang B, Woo T, Hu R, et al. Taxonomy of breast cancer based on normal cell phenotype predicts outcome. J Clin Invest. 2014;124(2):859-70. Epub 20140127. doi: 10.1172/JCI70941. PubMed PMID: 24463450; PubMed Central PMCID: PMCPMC3904619.

89. Granit RZ, Masury H, Condiotti R, Fixler Y, Gabai Y, Glikman T, et al. Regulation of Cellular Heterogeneity and Rates of Symmetric and Asymmetric Divisions in Triple-Negative Breast Cancer. Cell Rep. 2018;24(12):3237-50. Epub 2018/09/21. doi: 10.1016/j.celrep.2018.08.053. PubMed PMID: 30232005.

90. Allred DC. Issues and updates: evaluating estrogen receptor-alpha, progesterone receptor, and HER2 in breast cancer. Mod Pathol. 2010;23 Suppl 2:S52-9. Epub 2010/05/14. doi: 10.1038/modpathol.2010.55. PubMed PMID: 20436503.

91. McCaffrey LM, Macara IG. Epithelial organization, cell polarity and tumorigenesis. Trends Cell Biol. 2011;21(12):727-35. Epub 2011/07/26. doi: 10.1016/j.tcb.2011.06.005. PubMed PMID: 21782440.

92. Halaoui R, Rejon C, Chatterjee SJ, Szymborski J, Meterissian S, Muller WJ, et al. Progressive polarity loss and luminal collapse disrupt tissue organization in carcinoma. Genes Dev. 2017;31(15):1573-87. Epub 2017/09/10. doi: 10.1101/gad.300566.117. PubMed PMID: 28887414; PubMed Central PMCID: PMCPMC5630022.

93. Schenborn ET, Goiffon V. Calcium Phosphate Transfection of Mammalian Cultured Cells. In: Tymms MJ, editor. Transcription Factor Protocols. Totowa, NJ: Humana Press; 2000. p. 135-45.

94. Linnemann JR, Miura H, Meixner LK, Irmler M, Kloos UJ, Hirschi B, et al. Quantification of regenerative potential in primary human mammary epithelial cells. Development. 2015;142(18):3239-51. Epub 2015/06/14. doi: 10.1242/dev.123554. PubMed PMID: 26071498; PubMed Central PMCID: PMCPMC4582177.

95. McCaffrey LM, Macara IG. The Par3/aPKC interaction is essential for end bud remodeling and progenitor differentiation during mammary gland morphogenesis. Genes Dev. 2009;23(12):1450-60. Epub 2009/06/17. doi: 10.1101/gad.1795909. PubMed PMID: 19528321; PubMed Central PMCID: PMCPMC2701573.

96. Hubner NC, Mann M. Extracting gene function from protein-protein interactions using Quantitative BAC InteraCtomics (QUBIC). Methods. 2011;53(4):453-9. Epub 2010/12/28. doi: 10.1016/j.ymeth.2010.12.016. PubMed PMID: 21184827.

97. Smits AH, Jansen PW, Poser I, Hyman AA, Vermeulen M. Stoichiometry of chromatin-associated protein complexes revealed by label-free quantitative mass spectrometry-based proteomics. Nucleic Acids Res. 2013;41(1):e28. Epub 2012/10/16. doi: 10.1093/nar/gks941. PubMed PMID: 23066101; PubMed Central PMCID: PMCPMC3592467.

98. Szklarczyk D, Gable AL, Lyon D, Junge A, Wyder S, Huerta-Cepas J, et al. STRING v11: protein-protein association networks with increased coverage, supporting functional discovery in genome-wide experimental datasets. Nucleic Acids Res. 2019;47(D1):D607-D13. Epub 2018/11/27. doi: 10.1093/nar/gky1131. PubMed PMID: 30476243; PubMed Central PMCID: PMCPMC6323986.

99. Shannon P, Markiel A, Ozier O, Baliga NS, Wang JT, Ramage D, et al. Cytoscape: a software environment for integrated models of biomolecular interaction networks. Genome Res. 2003;13(11):2498-504. Epub 2003/11/05. doi: 10.1101/gr.1239303. PubMed PMID: 14597658; PubMed Central PMCID: PMCPMC403769.

100. Bindea G, Mlecnik B, Hackl H, Charoentong P, Tosolini M, Kirilovsky A, et al. ClueGO: a Cytoscape plug-in to decipher functionally grouped gene ontology and pathway annotation networks. Bioinformatics. 2009;25(8):1091-3. Epub 2009/02/25. doi: 10.1093/bioinformatics/btp101. PubMed PMID: 19237447; PubMed Central PMCID: PMCPMC2666812.

101. Schindelin J, Arganda-Carreras I, Frise E, Kaynig V, Longair M, Pietzsch T, et al. Fiji: an open-source platform for biological-image analysis. Nat Methods. 2012;9(7):676-82. Epub 2012/06/30. doi: 10.1038/nmeth.2019. PubMed PMID: 22743772; PubMed Central PMCID: PMCPMC3855844.

102. Boulanger J, Kervrann C, Bouthemy P, Elbau P, Sibarita JB, Salamero J. Patch-based nonlocal functional for denoising fluorescence microscopy image sequences. IEEE Trans Med Imaging. 2010;29(2):442-54. Epub 2009/11/11. doi: 10.1109/TMI.2009.2033991. PubMed PMID: 19900849.

103. di Pietro F, Valon L, Li Y, Goiame R, Genovesio A, Morin X. An RNAi Screen in a Novel Model of Oriented Divisions Identifies the Actin-Capping Protein Z beta as an Essential Regulator of Spindle Orientation. Curr Biol. 2017;27(16):2452-64 e8. Epub 2017/08/15. doi: 10.1016/j.cub.2017.06.055. PubMed PMID: 28803871.

104. French AP, Wilson MH, Kenobi K, Dietrich D, Voss U, Ubeda-Tomas S, et al. Identifying biological landmarks using a novel cell measuring image analysis tool: Cell-o-Tape. Plant Methods. 2012;8:7. Epub 2012/03/06. doi: 10.1186/1746-4811-8-7. PubMed PMID: 22385537; PubMed Central PMCID: PMCPMC3359173.

Fig 1

Fankhaenel *et al.*

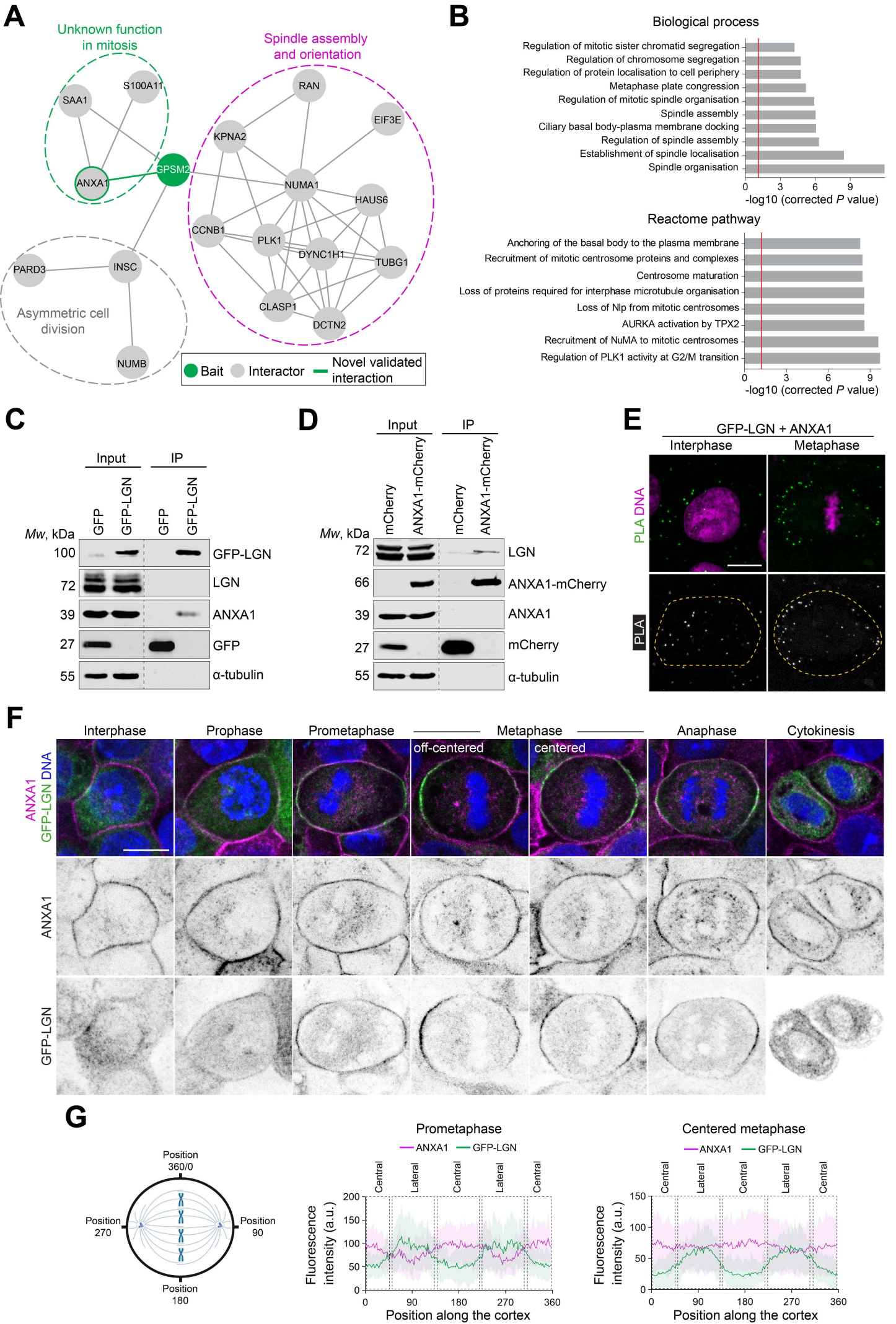

Fig 1. ANXA1 interacts with LGN at the cell cortex during mitosis. (A) Protein-protein interaction network of LGN (GPSM2, red) showing several interactors (grey) of known and unknown mitotic functions. The green line highlights a novel interaction between LGN and ANXA1, which is further validated in this study. **(B)** Gene Ontology analysis of the LGN network presenting terms from Biological process (left) and Reactome pathway analysis (right) significantly enriched. *P*-values were derived from the hypergeometric test (Fisher's Exact Test) with Bonferroni step-down correction from multiple tests. **(C)** ANXA1 and GFP-LGN co-immunoprecipitate from clonal MCF-10A stably expressing GFP-LGN, arrested in metaphase. Lysates were subjected to affinity purification with GFP-Trap beads. The immunoprecipitates (IP) were analysed by western blotting. **(D)** LGN and ANXA1-mCherry co-immunoprecipitate from clonal MCF-10A cells stably expressing ANXA1-mCherry, arrested in metaphase. Lysates were subjected to affinity purification with RFP-Trap beads. The immunoprecipitates were analysed by western blotting. **(E)** Proximity ligation assay (PLA) performed using GFP and ANXA1 antibodies in GFP-LGN-expressing MCF10A cells. Cells were counterstained with DAPI (DNA, magenta). Green dotted lines indicate the cell contour. **(F)** Confocal images of representative clonal MCF-10A cells stably expressing GFP-LGN (green) stained for ANXA1 (magenta) and counterstained with DAPI (DNA, blue). **(G)** Average cortical fluorescence intensity profiles of GFP-LGN and ANXA1 in prometaphase cells (left) and metaphase cells (right) from 3 independent experiments (prometaphase n = 33 cells; metaphase n = 36 cells). Positions along the cortex in the graphs correspond to coordinates as illustrated in the schematic. All scale bars, 10 μm.

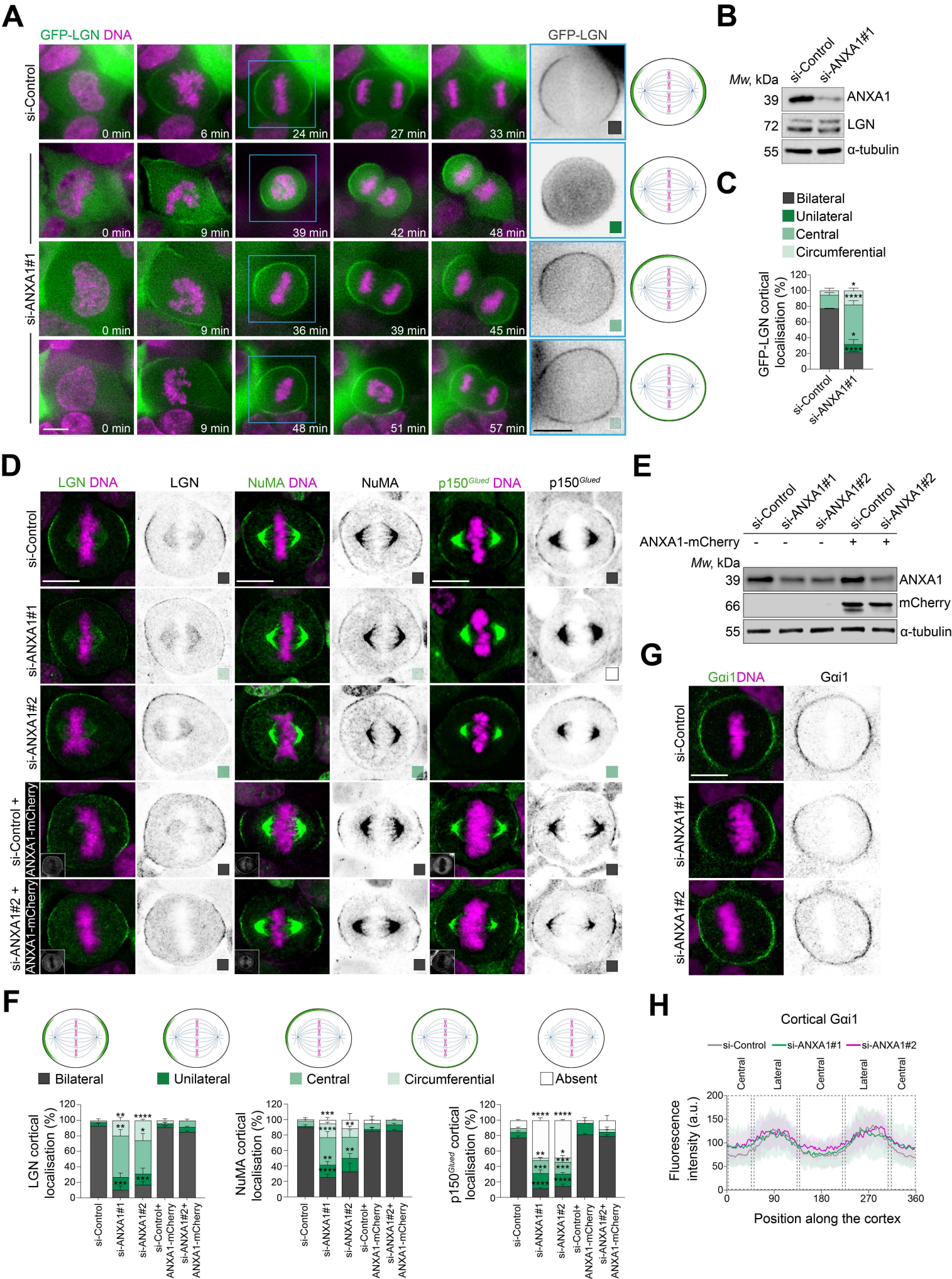
A
GFP-LGN DNA
GFP-LGN
si-Control
si-ANXA1#1
0 min
6 min
24 min
27 min
33 min
9 min
39 min
42 min
48 min
36 min
45 min
51 min
57 min
B
Mw, kDa
si-Control
si-ANXA1#1
39
72
55
ANXA1
LGN
α-tubulin
C
Bilateral
Unilateral
Central
Circumferential
GFP-LGN cortical localisation (%)
D
LGN DNA
LGN
NuMA DNA
NuMA
p150Glued DNA
p150Glued
si-ANXA1#2
si-Control + ANXA1-mCherry
si-ANXA1#2 + ANXA1-mCherry
E
ANXA1-mCherry
66
mCherry
G
Gαi1DNA
Gαi1
F
Absent
LGN cortical localisation (%)
NuMA cortical localisation (%)
p150Glued cortical localisation (%)
H
Cortical Gαi1
Central
Lateral
Fluorescence intensity (a.u.)
Position along the cortex

Fig 2. ANXA1 is required for correct localisation of the LGN-NuMA-Dynein-Dynactin complex at the cell cortex during mitosis. (A) Left: time-lapse images of representative clonal MCF-10A cells stably expressing GFP-LGN (green), treated with si-Control or si-ANXA1#1. DNA is stained with Hoechst 33342 (magenta) 30 min before imaging. Right: illustration showing the observed cortical localisation of GFP-LGN **(B)** Western blotting of extracts from siRNA-transfected cells. **(C)** Percentage of cortical localisation of GFP-LGN in siRNA-transfected cells (si-Control: n = 53 cells; si-ANXA1#1: n = 41 cells). **(D)** Confocal images of representative si-Control-, si-ANXA1#1 and si-ANXA1#2-transfected metaphase cells expressing or not ANXA1-mCherry and stained for LGN, NuMA or p150^{Glued} (green) and counterstained with DAPI (DNA, magenta). **(E)** Western blotting of extracts from siRNA-transfected cells expressing or not ANXA1-mCherry. **(F)** Percentage of cortical localisation of LGN, NuMA or p150^{Glued} in siRNA-transfected metaphase cells expressing or not ANXA1-mCherry: LGN (si-Control: n = 70 cells; si-ANXA1: n = 51 cells; si-ANXA1#2: n = 43 cells; si-Control + ANXA1-mCherry: n = 30 cells; si-ANXA1#2 + ANXA1-mCherry: n = 30 cells), NuMA (si-Control n = 73; si-ANXA1 n = 62; si-ANXA1#2 n = 45; si-Control + ANXA1-mCherry: n = 30 cells; si-ANXA1#2 + ANXA1-mCherry: n = 30 cells), p150^{Glued} (si-Control n = 79; si-ANXA1 n = 101; si-ANXA1#2 n = 99; si-Control + ANXA1-mCherry: n = 30 cells; si-ANXA1#2 + ANXA1-mCherry: n = 30 cells). **(G)** Confocal images of representative si-Control-, si-ANXA1#1- and si-ANXA1#2-treated metaphase cells stained for $G_{\alpha i1}$ (green) and counterstained with DAPI (DNA, magenta). **(H)** Average cortical fluorescence intensity profiles of $G_{\alpha i1}$ in siRNA-transfected metaphase cells (si-Control: n = 32; si-ANXA1#1: n = 30; si-ANXA1#2: n = 30). All data are presented as means ± s.e.m. from 3 independent experiments. * $P \leq 0.05$, ** $P \leq 0.01$, *** $P \leq 0.001$, **** $P \leq 0.0001$ (one-way ANOVA; *t*-test). All scale bars, 10 μm.

Fig 3

Fankhaenel *et al.*

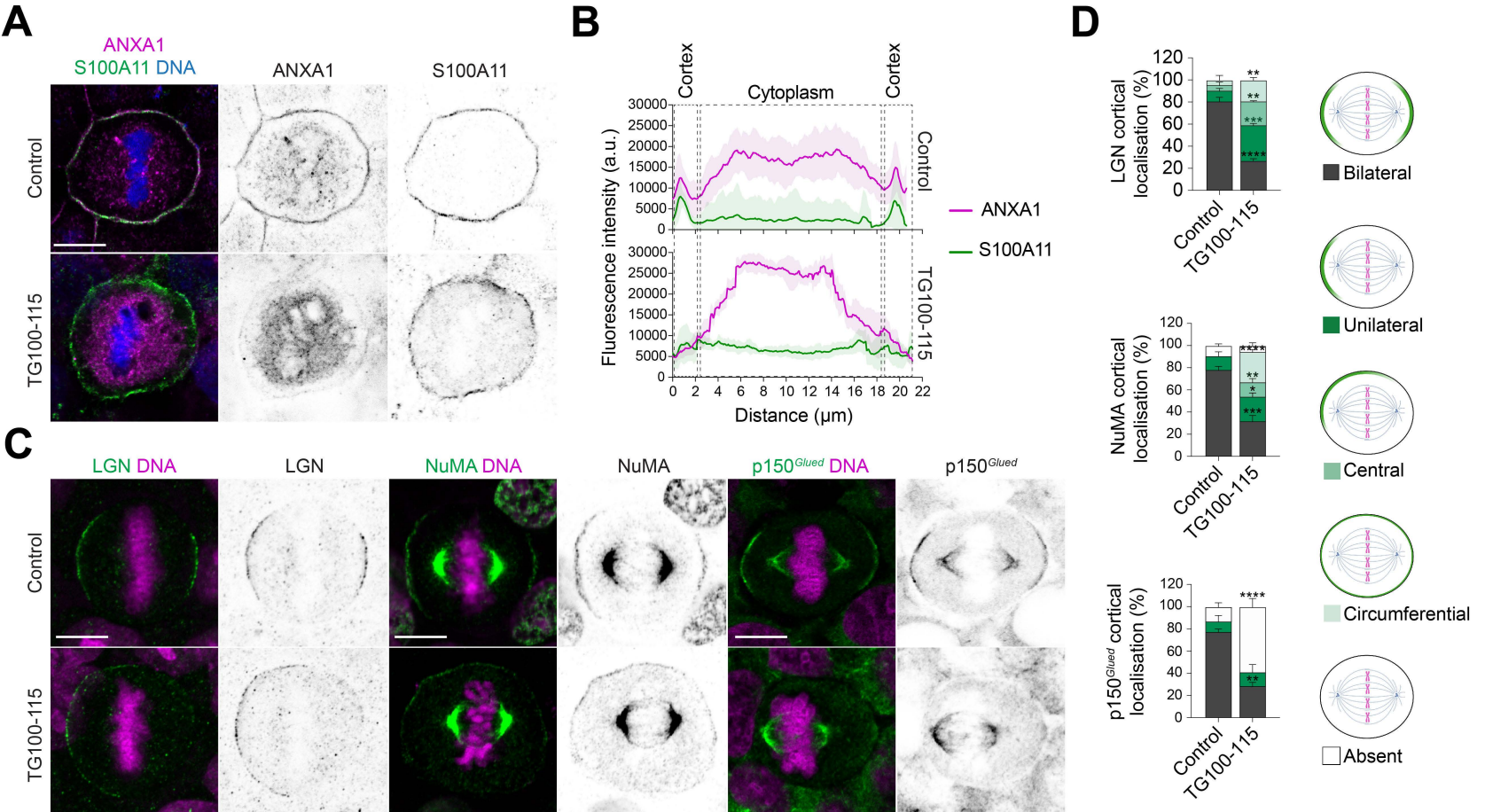

Fig 3. ANXA1 localisation to the plasma membrane is required for the patterning of LGN-NuMA-Dynein-Dynactin at the lateral cortex during metaphase. (A) Confocal images of representative MCF-10A cells treated with DMSO (Control) or 20 μM TG100-115 for 2h, stained for ANXA1 (magenta) and S100A11 (green), and counterstained with DAPI (DNA, blue). **(B)** Average cortical and cytoplasmic fluorescence intensity profiles of ANXA1 and S100A11 from metaphase cells (Control: n = 30; TG100-115: n = 30). **(C)** Confocal images of representative MCF-10A cells treated with DMSO (Control) or 20 μM TG100-115 for 2h, stained for LGN, NuMA or p150^{Glued} (green), and counterstained with DAPI (DNA, magenta). **(D)** Percentage of cortical localisation of LGN, NuMA or p150^{Glued} in Control and TG100-115-treated metaphase cells: LGN (Control: n = 30 cells; TG100-115: n = 30), NuMA (Control: n = 30 cells; TG100-115: n = 30), p150^{Glued} (Control: n = 30 cells; TG100-115: n = 30). All data are presented as means ± s.e.m. from 3 independent experiments. * $P \leq 0.05$, ** $P \leq 0.01$, *** $P \leq 0.001$, **** $P \leq 0.0001$ (one-way ANOVA). All scale bar, 10 μm.

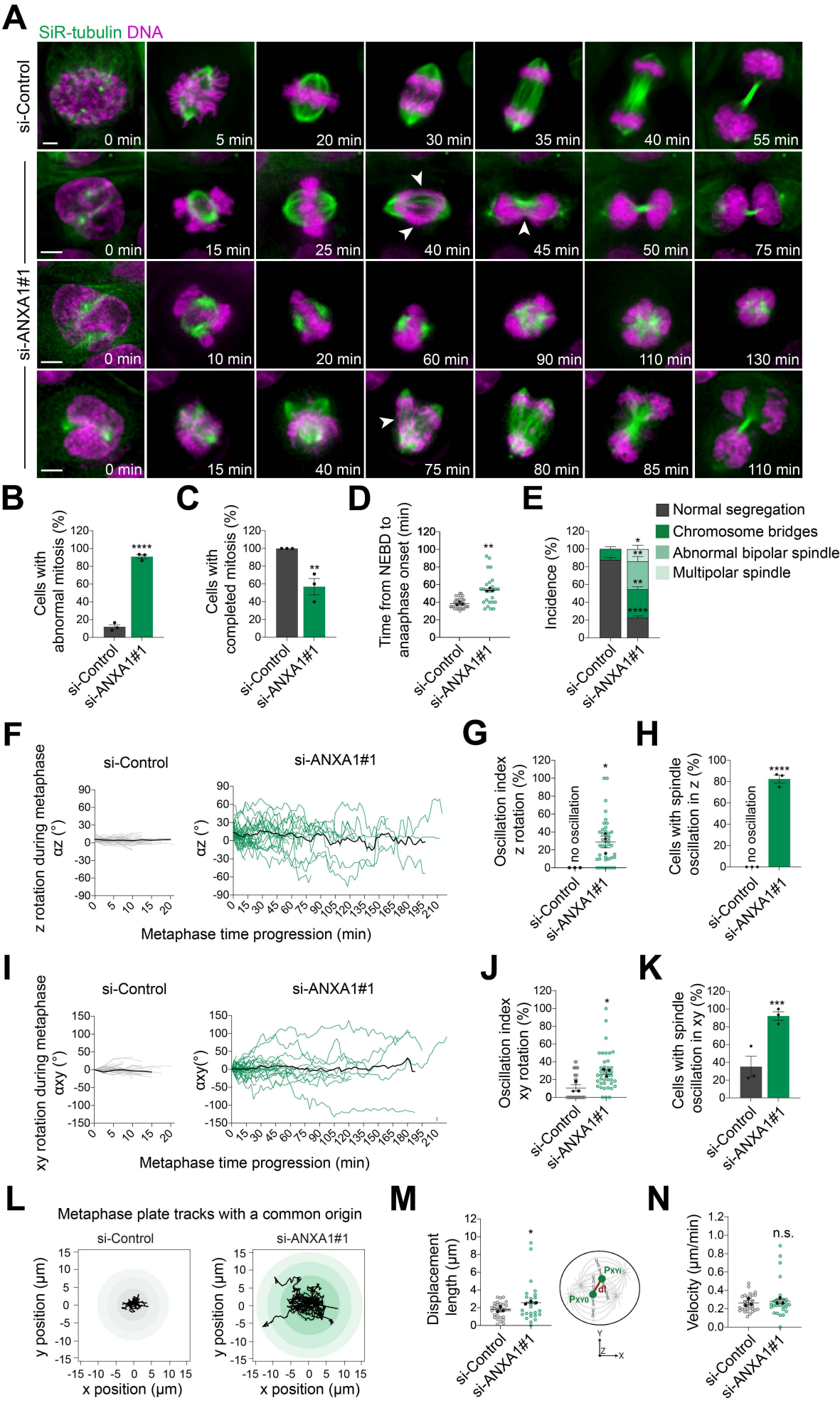
A
SiR-tubulin DNA
si-Control
si-ANXA1#1
0 min
5 min
20 min
30 min
35 min
40 min
55 min
0 min
15 min
25 min
40 min
45 min
50 min
75 min
0 min
10 min
20 min
60 min
90 min
110 min
130 min
0 min
15 min
40 min
75 min
80 min
85 min
110 min
B
Cells with abnormal mitosis (%)
si-Control
si-ANXA1#1
C
Cells with completed mitosis (%)
D
Time from NEBD to anaaphase onset (min)
E
Incidence (%)
Normal segregation
Chromosome bridges
Abnormal bipolar spindle
Multipolar spindle
F
si-Control
si-ANXA1#1
z rotation during metaphase
αz (°)
Metaphase time progression (min)
G
Oscillation index z rotation (%)
no oscillation
H
Cells with spindle oscillation in z (%)
I
si-Control
si-ANXA1#1
xy rotation during metaphase
αxy (°)
Metaphase time progression (min)
J
Oscillation index xy rotation (%)
K
Cells with spindle oscillation in xy (%)
L
Metaphase plate tracks with a common origin
si-Control
si-ANXA1#1
y position (µm)
x position (µm)
M
Displacement length (µm)
Pxyi
Pxyo
dt
N
Velocity (µm/min)
n.s.

Fig 4. ANXA1 is required for correct mitotic progression and spindle dynamics. (A) Time-lapse images of representative MCF-10A cells treated with si-Control or si-ANXA1#1. Microtubules are labelled with SiR-tubulin (green) and DNA with Hoechst 33342 (magenta), 2h and 30 min before acquisition, respectively. Arrowheads indicate the phenotypes listed in (e). Scale bars, 5 μm. **(B)** Percentage of cells with abnormal mitosis in siRNA-transfected cells. **(C)** Percentage of cells that completed mitosis in siRNA-treated cells. **(D)** Time from nuclear envelope breakdown (NEBD) to anaphase onset in siRNA-transfected cells. **(E)** Percentage of chromosomes segregation and spindle assembly defects in siRNA-transfected cells. **(F)** Dynamics of z orientation (αz) during metaphase in si-Control- (left) and si-ANXA1#1-treated (right) cells. Black lines represent the average spindle angles of all analysed cells. **(G)** Oscillation index in siRNA-transfected cells, representing the frequency at which mitotic spindle position changes > 10° between two successive frames in the z axis. **(H)** Percentage of cells with spindle oscillations in the z axis in siRNA-transfected cells. **(I)** Dynamics of xy orientation (αxy) during metaphase in si-Control- (left) and si-ANXA1#1-transfected (right) cells. Black lines represent the average spindle angles of all analysed cells. **(J)** Oscillation index in si-Control- and si-ANXA1#1-transfected cells, representing the frequency at which mitotic spindle position changes > 10° between two successive frames in the xy axis. **(K)** Percentage of cells with spindle oscillations in the xy axis in siRNA-transfected cells. **(L)** Origin-aligned metaphase plate tracks in the xy plane of si-Control- (left) and si-ANXA1#1-transfected (right) cells. Black lines correspond to individual cells. **(M)** Displacement length from the starting point to the position at the end of metaphase in siRNA-transfected cells. **(N)** Velocity of metaphase plate movements in si-RNA-transfected, calculated by dividing the track length by metaphase duration. All data are presented as means ± s.e.m. from 3 independent experiments (si-Control: n = 33 cells; si-ANXA1#1: n = 44; si-ANXA1#2: n = 35 cells). * $P \leq 0.05$, ** $P \leq 0.01$, *** $P \leq 0.001$, **** $P \leq 0.0001$, n.s. (not significant) (*t*-test).

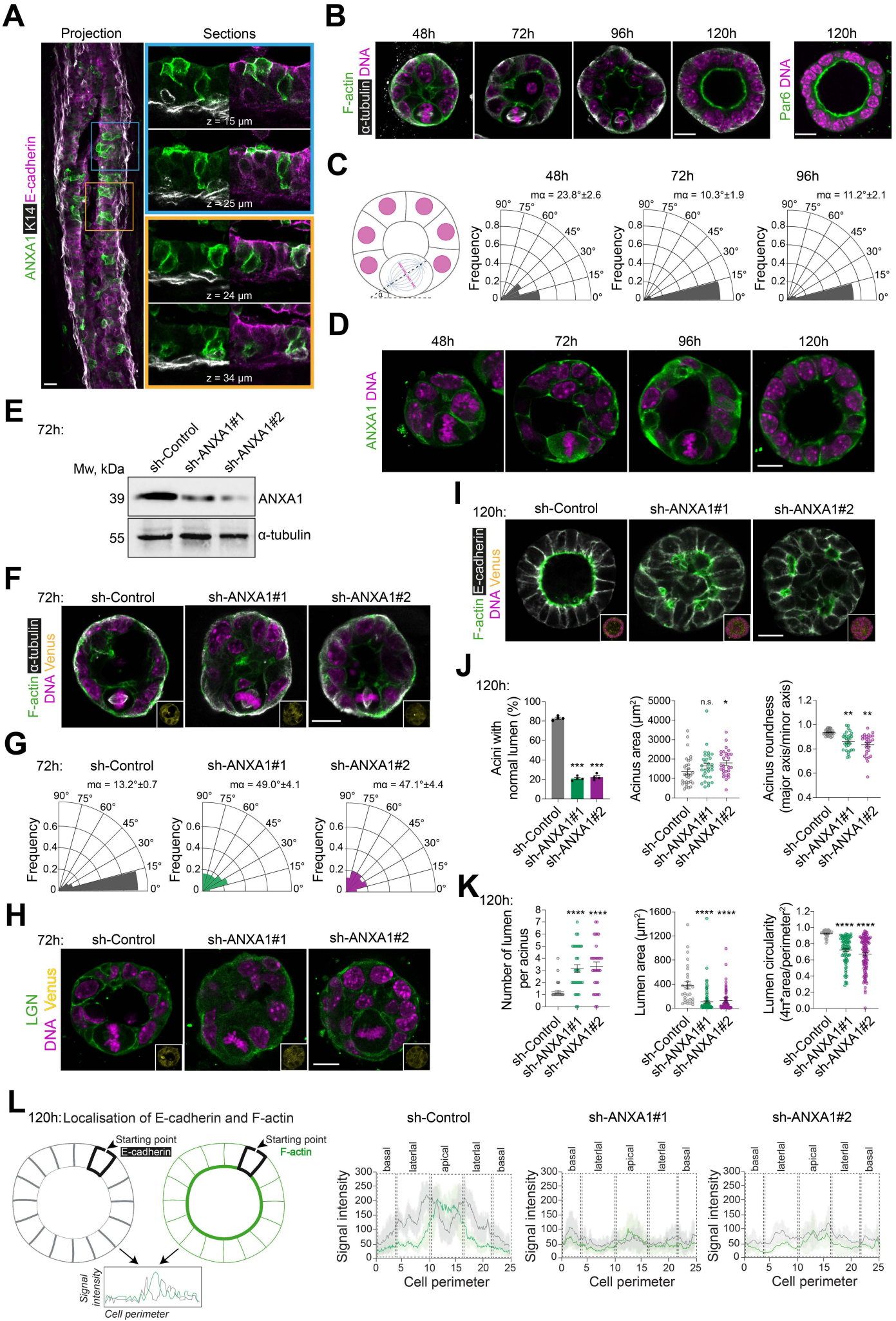
A
Projection
Sections
ANXA1 K14 E-cadherin
z = 15 µm
z = 25 µm
z = 24 µm
z = 34 µm
B
48h
72h
96h
120h
F-actin α-tubulin DNA
120h
Par6 DNA
C
48h
72h
96h
mα = 23.8°±2.6
mα = 10.3°±1.9
mα = 11.2°±2.1
Frequency
D
48h
72h
96h
120h
ANXA1 DNA
E
72h:
sh-Control
sh-ANXA1#1
sh-ANXA1#2
Mw, kDa
39
55
ANXA1
α-tubulin
F
72h:
sh-Control
sh-ANXA1#1
sh-ANXA1#2
F-actin α-tubulin DNA Venus
G
72h:
sh-Control
sh-ANXA1#1
sh-ANXA1#2
mα = 13.2°±0.7
mα = 49.0°±4.1
mα = 47.1°±4.4
Frequency
H
72h:
sh-Control
sh-ANXA1#1
sh-ANXA1#2
LGN DNA Venus
I
120h:
sh-Control
sh-ANXA1#1
sh-ANXA1#2
F-actin E-cadherin DNA Venus
J
120h:
Acini with normal lumen (%)
Acinus area (µm²)
Acinus roundness (major axis/minor axis)
n.s.
*
**
***
sh-Control
sh-ANXA1#1
sh-ANXA1#2
K
120h:
Number of lumen per acinus
Lumen area (µm²)
Lumen circularity (4π*area/perimeter²)
****
sh-Control
sh-ANXA1#1
sh-ANXA1#2
L
120h: Localisation of E-cadherin and F-actin
Starting point
E-cadherin
Starting point
F-actin
Signal intensity
Cell perimeter
sh-Control
sh-ANXA1#1
sh-ANXA1#2
basal
laterial
apical
laterial
basal
Signal intensity
Cell perimeter

Fig 5. ANXA1 is required for correct mitotic spindle orientation during 3D morphogenesis. (A) Confocal images of representative mouse mammary gland cryosections (50 µm-thick) stained for ANXA1 (green), K14 (grey) and E-cadherin (magenta). **(B)** Confocal images of representative mMEC acini stained for F-actin (green) and α-tubulin (grey) or Par6 (green) and counterstained with DAPI (DNA, magenta). **(C)** Spindle angle frequencies and mean angles (mα) (48h: n = 42 acini; 72h: n = 40 acini; 96h: n = 39 acini). **(D)** Confocal images of representative acini stained for ANXA1 (green) and counterstained with DAPI (DNA, magenta). **(E)** Western blotting of extracts from shRNA-transduced acini. **(F)** Confocal images of representative shRNA-transduced acini (Venus, yellow) stained for F-actin (green) and α-tubulin (grey) and counterstained with DAPI (DNA, magenta). **(G)** Spindle angle frequencies and mean angles (mα) (sh-Control: n = 30 acini; sh-ANXA1#1: n = 30 acini; sh-ANXA1#2: n = 30 acini). **(H)** Confocal images of representative shRNA-transduced acini (Venus, yellow) stained for LGN (green) and counterstained with DAPI (DNA, magenta). **(I)** Confocal images of representative shRNA-transduced acini (Venus, yellow) stained for F-actin (green) and E-cadherin (grey) and counterstained with DAPI (DNA, magenta). **(J)** Quantification of the percentage of acini with normal lumen (left) (sh-Control: n = 163 acini; sh-ANXA1#1: n = 142 acini; sh-ANXA1#2: n = 168 acini), acinus area (middle) and acinus roundness (right) (sh-Control: n = 30 acini; sh-ANXA1#1: n = 30 acini; sh-ANXA1#2: n = 30 acini). **(K)** Quantification of the number of lumen per acinus (left), lumen area (middle) and lumen circularity (right) (sh-Control: n = 30; sh-ANXA1#1: n = 30; sh-ANXA1#2: n = 30). **(L)** Left: illustration showing quantification of cortical fluorescence intensity of F-actin (green) and E-cadherin (grey) in acini. Right: average cortical fluorescence intensity profiles of E-cadherin and F-actin (sh-Control: n = 30; sh-ANXA1#1: n = 30; sh-ANXA1#2: n = 30). All time-points of 3D culture are indicated in hours (h). All data are presented as means ± s.e.m. from at least 3 independent experiments. * $P \leq 0.05$, ** $P \leq 0.01$, *** $P \leq 0.001$ **** $P \leq 0.0001$, n.s. (not significant) (Kolmogorov-Smirnov test; one-way ANOVA; *t*-test). All scale bars, 10 µm.

Fig 6

Fankhaenel *et al.*

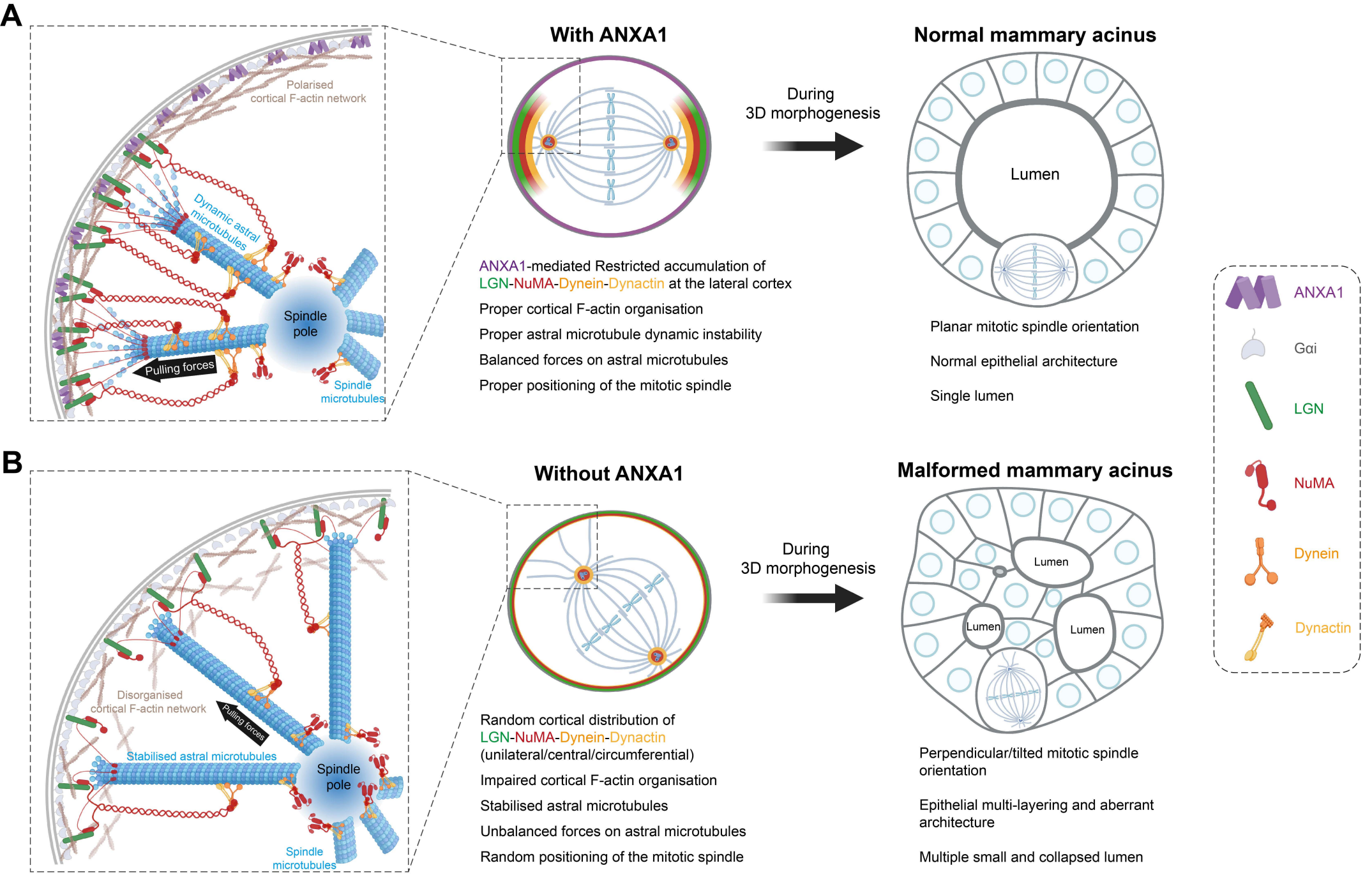

Fig 6. Proposed model for ANXA1 regulation of planar mitotic spindle orientation and epithelial morphogenesis. (A) Cortical ANXA1 interacts with LGN to instruct polarised accumulation of the LGN-NuMA complex at the lateral cortex. NuMA in turn, recruits Dynein-Dynactin generating pulling forces on the spindle poles that are balanced by ANXA1-dependent regulation of cortical F-actin and astral microtubule organisation, thereby ensuring planar alignment of the mitotic spindle. During 3D morphogenesis, ANXA1-dependent regulation of planar mitotic spindle orientation is crucial for single lumen formation and normal epithelial architecture. **(B)** Loss of ANXA1 results in a diffuse cortical distribution of LGN and NuMA, which in turn impairs the recruitment of Dynein-Dynactin to the cell cortex. This affects the length and dynamic instability of astral microtubules as well as cortical F-actin integrity, generating unbalanced forces that result in randomised mitotic spindle orientation. During 3D morphogenesis, mitotic spindle misorientation upon ANXA1 knockdown results in epithelial multi-layering, leading to multi-lumen formation and aberrant epithelial architecture.

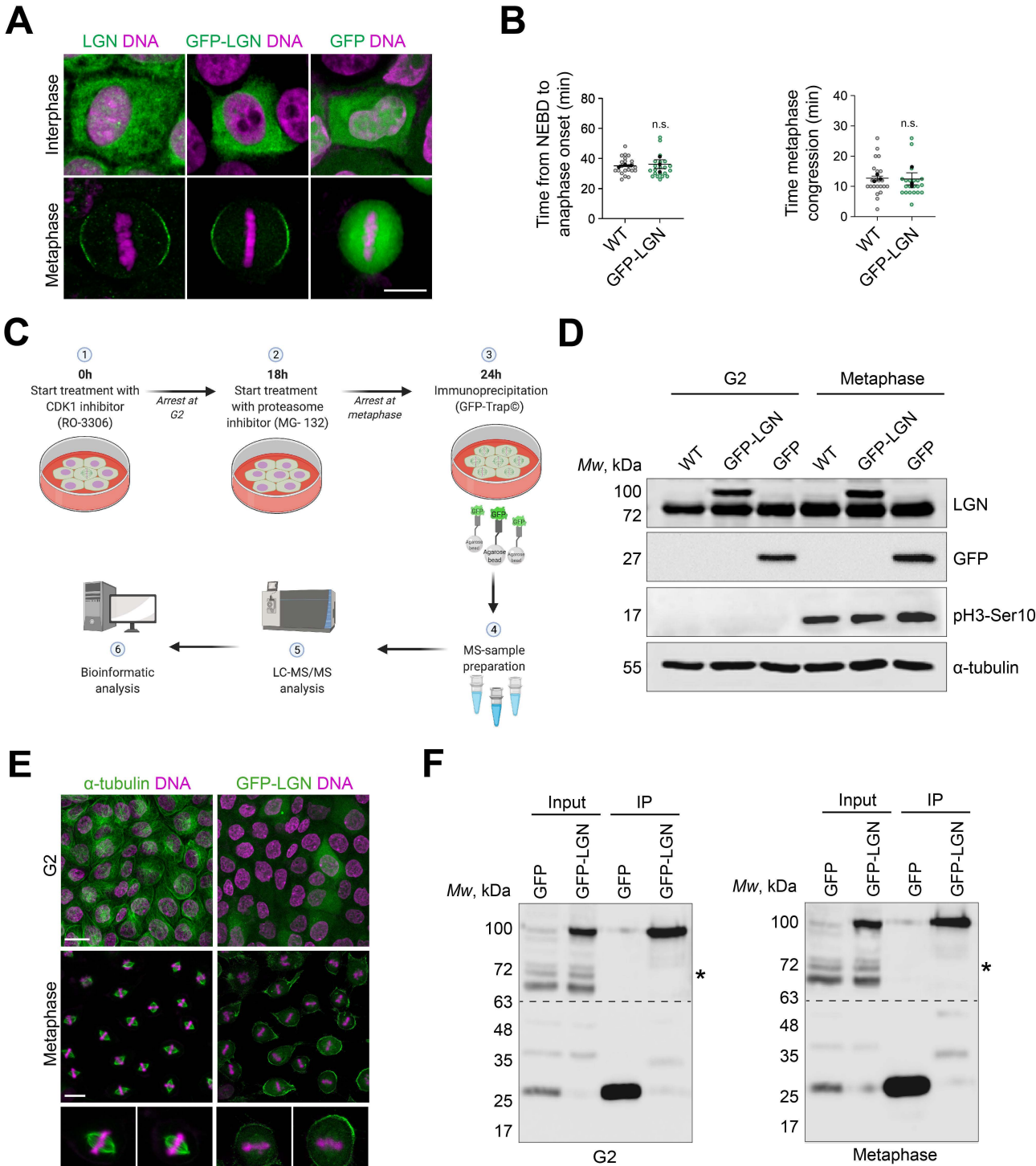
A
LGN DNA
GFP-LGN DNA
GFP DNA
Interphase
Metaphase
B
Time from NEBD to anaphase onset (min)
80
60
40
20
0
n.s.
WT
GFP-LGN
Time metaphase congression (min)
40
30
20
10
0
n.s.
WT
GFP-LGN
C
1
0h
Start treatment with CDK1 inhibitor (RO-3306)
Arrest at G2
2
18h
Start treatment with proteasome inhibitor (MG- 132)
Arrest at metaphase
3
24h
Immunoprecipitation (GFP-Trap©)
Agarose bead
4
MS-sample preparation
5
LC-MS/MS analysis
6
Bioinformatic analysis
D
G2
Metaphase
WT
GFP-LGN
GFP
WT
GFP-LGN
GFP
Mw, kDa
100
72
LGN
27
GFP
17
pH3-Ser10
55
α-tubulin
E
α-tubulin DNA
GFP-LGN DNA
G2
Metaphase
F
Input
IP
GFP
GFP-LGN
GFP
GFP-LGN
Mw, kDa
100
72
63
48
35
25
17
*
G2
Input
IP
GFP
GFP-LGN
GFP
GFP-LGN
Mw, kDa
100
72
63
48
35
25
17
*
Metaphase

Fig S1. Experimental design for determining the LGN interactome in mammary epithelial cells. (A) Confocal images of representative wild type (WT) MCF-10A and the generated clonal MCF-10A stably expressing GFP-LGN or GFP in interphase and metaphase. Cells are stained for LGN or GFP (green) and counterstained with DAPI (DNA, magenta). **(B)** Time from NEBD to anaphase (left) and duration of metaphase congression (right), determined from time-lapse microscopy in WT MCF-10A cells and clonal MCF-10A stably expressing GFP-LGN (WT n = 21; GFP-LGN n = 23). **(C)** Illustration showing the proteomic workflow from the synchronisation procedure to the experimental pipeline leading to LC-MS/MS and bioinformatic-based identification of the LGN interactome. Cells were treated with the CDK1 inhibitor RO-3306, yielding cells synchronised in G2 phase, then arrested in metaphase by treatment with the proteasome inhibitor MG-132. The drugs used for synchronisation were washed out prior to extract preparation for affinity purification with GFP-Trap beads. **(D)** Western blotting of extracts from WT MCF-10A and clonal MCF-10A stably expressing GFP-LGN or GFP cells synchronised in G2 phase or metaphase. **(E)** Confocal images of representative clonal MCF-10A stably expressing GFP-LGN cells synchronised in G2 phase or metaphase. Cells are stained for α-tubulin or GFP (green) and counterstained with DAPI (DNA, magenta). **(F)** Western blotting of extracts of GFP- and GFP-LGN-bead-bound elutions from cells synchronised in G2 phase (left) or metaphase (right). Asterisks indicate endogenous LGN in the input samples. All data are presented as means ± s.e.m. from 3 independent experiments. n.s. (not significant, *t*-test). All scale bars, 10 μm.

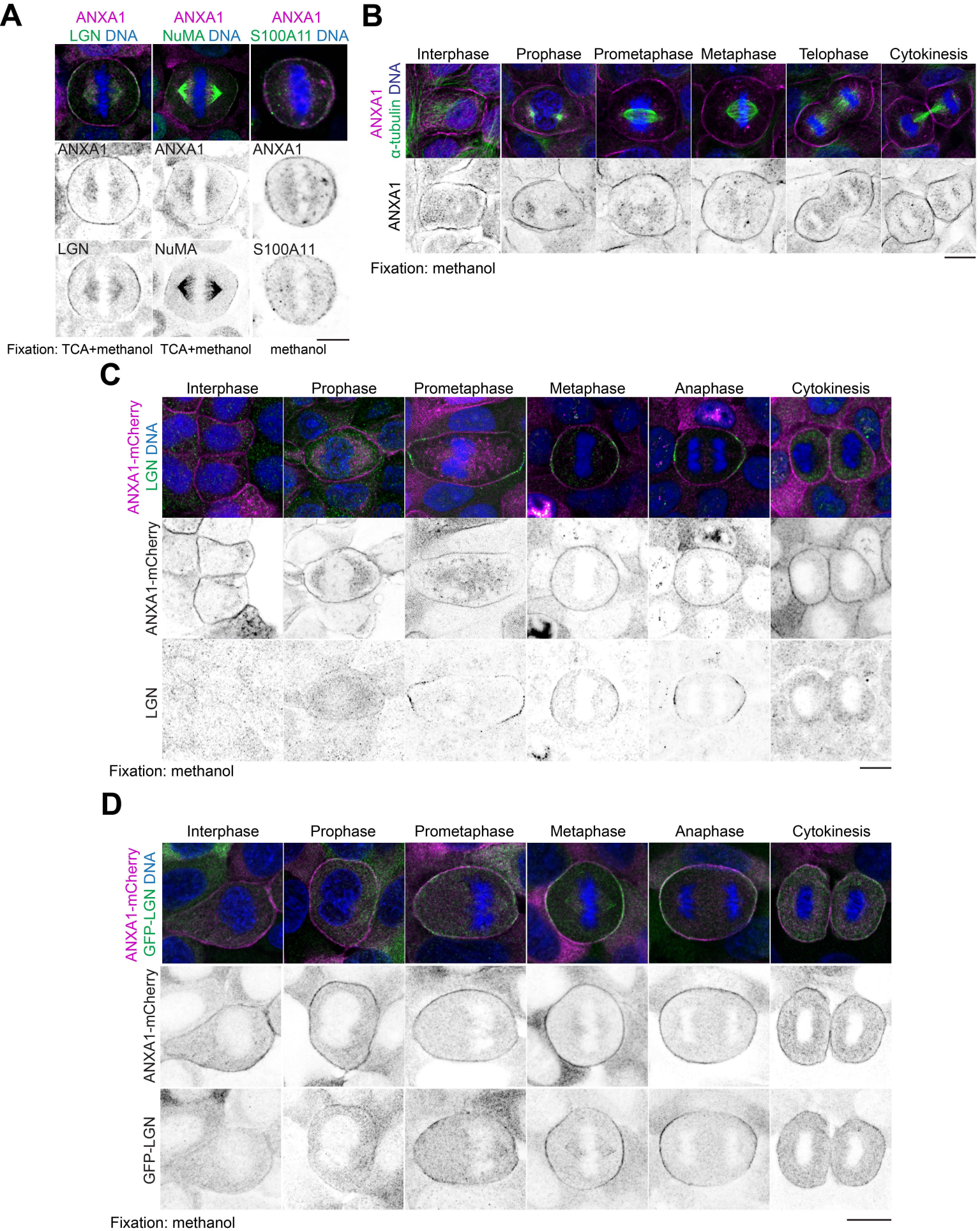
A
ANXA1
LGN DNA
ANXA1
NuMA DNA
ANXA1
S100A11 DNA
ANXA1
ANXA1
ANXA1
LGN
NuMA
S100A11
Fixation: TCA+methanol
TCA+methanol
methanol
B
Interphase
Prophase
Prometaphase
Metaphase
Telophase
Cytokinesis
ANXA1
α-tubulin DNA
ANXA1
Fixation: methanol
C
Interphase
Prophase
Prometaphase
Metaphase
Anaphase
Cytokinesis
ANXA1-mCherry
LGN DNA
ANXA1-mCherry
LGN
Fixation: methanol
D
Interphase
Prophase
Prometaphase
Metaphase
Anaphase
Cytokinesis
ANXA1-mCherry
GFP-LGN DNA
ANXA1-mCherry
GFP-LGN
Fixation: methanol

Fig S2. ANXA1 co-distributes with S100A11, LGN, NuMA, and microtubules. (A) Confocal images of representative MCF-10A cells stained for ANXA1 (magenta) and LGN, NuMA or S100A11 (green), and counterstained with DAPI (DNA, blue). **(B)** Confocal images of representative MCF-10A stained for ANXA1 (magenta) and α-tubulin (green), and counterstained with DAPI (DNA, blue). **(C)** Confocal images of representative clonal MCF-10A cells stably expressing ANXA1-mCherry (magenta) stained for LGN (green) and counterstained with DAPI (DNA, blue). **(D)** Confocal images of representative clonal MCF-10A cells stably expressing ANXA1-mCherry (magenta) and GFP-LGN (green) and counterstained with DAPI (DNA, blue). All scale bar, 10 μm.

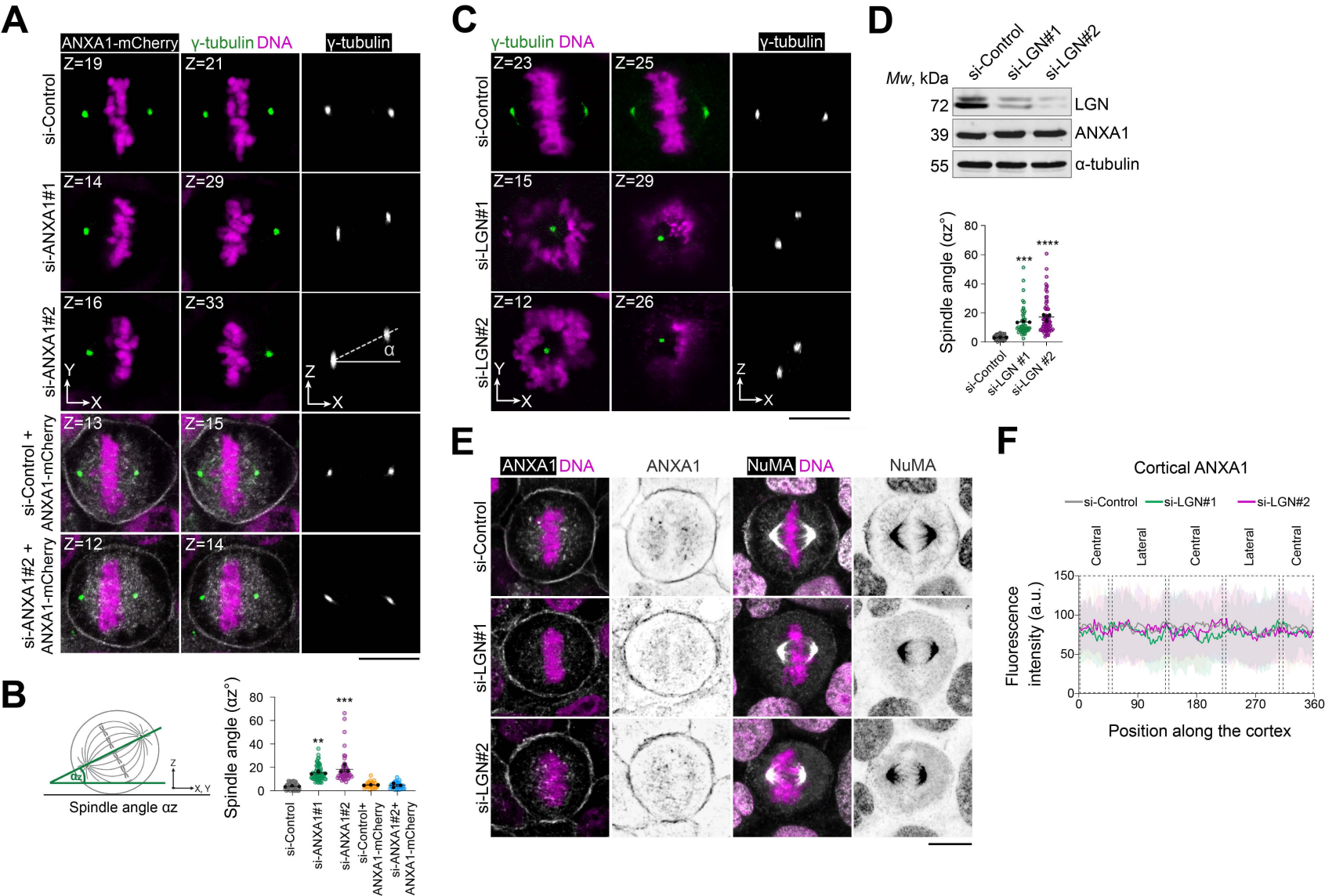
A
ANXA1-mCherry
γ-tubulin DNA
γ-tubulin
si-Control
si-ANXA1#1
si-ANXA1#2
si-Control + ANXA1-mCherry
si-ANXA1#2 + ANXA1-mCherry
Z=19
Z=21
Z=14
Z=29
Z=16
Z=33
Z=13
Z=15
Z=12
Z=14
Y
X
Z
α
B
Spindle angle αz
Spindle angle (αz°)
si-Control
si-ANXA1#1
si-ANXA1#2
si-Control+ ANXA1-mCherry
si-ANXA1#2+ ANXA1-mCherry
C
γ-tubulin DNA
γ-tubulin
si-Control
si-LGN#1
si-LGN#2
Z=23
Z=25
Z=15
Z=29
Z=12
Z=26
D
Mw, kDa
si-Control
si-LGN#1
si-LGN#2
72
39
55
LGN
ANXA1
α-tubulin
Spindle angle (αz°)
E
ANXA1 DNA
ANXA1
NuMA DNA
NuMA
si-Control
si-LGN#1
si-LGN#2
F
Cortical ANXA1
si-Control
si-LGN#1
si-LGN#2
Central
Lateral
Central
Lateral
Central
Fluorescence intensity (a.u.)
Position along the cortex

Fig S3. ANXA1 acts upstream of LGN to ensure proper mitotic spindle orientation. (A) Confocal images of representative MCF-10A cells transfected with si-Control, si-ANXA1#1 or si-ANXA1#2, expressing or not ANXA1-mCherry and stained for γ-tubulin (green), and counterstained with DAPI (DNA, magenta). Z projections in the XY view and XZ view are shown. Scale bars, 5 µm. **(B)** Mitotic spindle angles in siRNA-transfected cells expressing or not ANXA1-mCherry (si-Control: n = 71; si-ANXA1#1: n = 65; si-ANXA1#2: n = 49; si-Control + ANXA1-mCherry: n = 30; si-ANXA1#2 + ANXA1-mCherry: n= 30). **(C)** Confocal images of representative MCF-10A cells transfected with si-Control, si-LGN#1 or si-LGN#2 stained for γ-tubulin (green) and counterstained with DAPI (DNA, magenta). Z projections in the XY view and XZ view are shown. Scale bars, 5 µm. **(D)** Top: Western blotting of extracts from MCF-10A transfected with si-Control, si-LGN#1 or si-LGN#2. Bottom: Mitotic spindle angles in siRNA-transfected cells (si-Control n = 68; si-LGN#1 n = 50; si-LGN#2 n = 67). **(E)** Confocal images of representative MCF-10A cells stained for ANXA1 or NuMA (grey) and counterstained with DAPI (DNA, magenta). Scale bars, 10 µm. **(F)** Average cortical fluorescence intensity profiles of ANXA1 from metaphase siRNA-transfected cells (si-Control n = 41; si-LGN#1 n = 26; si-LGN#2 n = 25). All data are presented as means ± s.e.m. from 3 independent experiments. ** $P \leq 0.01$, *** $P \leq 0.001$ **** $P \leq 0.0001$ (one-way ANOVA).

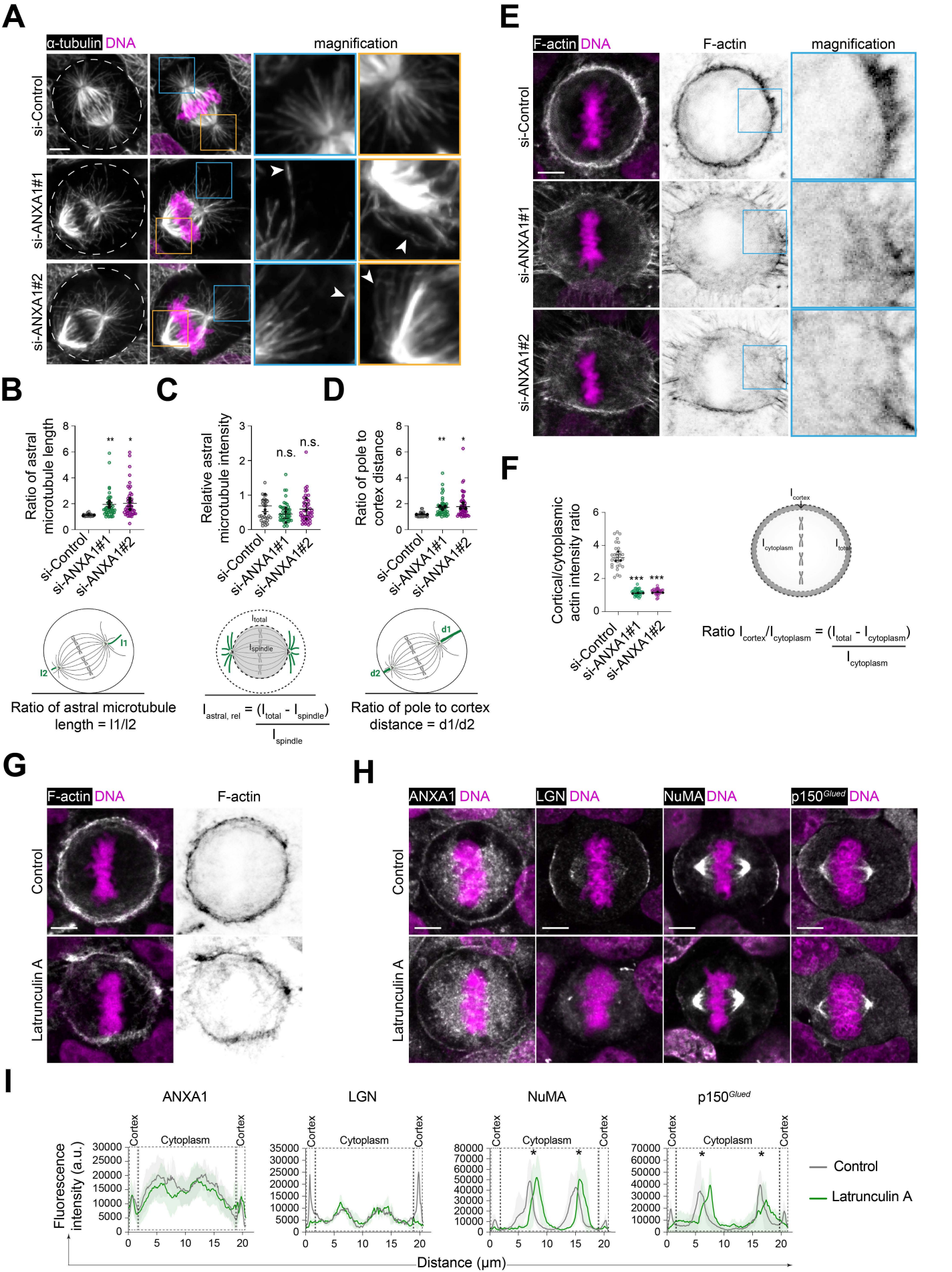
A
α-tubulin DNA
magnification
si-Control
si-ANXA1#1
si-ANXA1#2
B
Ratio of astral microtubule length
si-Control
si-ANXA1#1
si-ANXA1#2
Ratio of astral microtubule length = l1/l2
C
Relative astral microtubule intensity
n.s.
n.s.
$I_{astral, rel} = \frac{(I_{total} - I_{spindle})}{I_{spindle}}$
D
Ratio of pole to cortex distance
Ratio of pole to cortex distance = d1/d2
E
F-actin DNA
F-actin
magnification
F
Cortical/cytoplasmic actin intensity ratio
Ratio $I_{cortex}/I_{cytoplasm} = \frac{(I_{total} - I_{cytoplasm})}{I_{cytoplasm}}$
G
F-actin DNA
F-actin
Control
Latrunculin A
H
ANXA1 DNA
LGN DNA
NuMA DNA
p150Glued DNA
Control
Latrunculin A
I
ANXA1
LGN
NuMA
p150Glued
Cortex
Cytoplasm
Fluorescence intensity (a.u.)
Distance (µm)
Control
Latrunculin A

Fig S4. Interplay between ANXA1, LGN-NuMA, astral microtubules and cortical F-actin during metaphase. (A) Confocal images of representative metaphase MCF-10A cells transfected with si-Control, si-ANXA1#1 or si-ANXA1#2 stained for α-tubulin (grey) and counterstained with DAPI (DNA, magenta). Insets show magnified images of framed regions. White arrowheads indicate elongated and buckled astral microtubules. Dashed lines outline the cell contour. **(B)** Ratio of astral microtubule length (l) in siRNA-transfected cells (si-Control n = 31; si-ANXA1#1 n = 46; si-ANXA1#2 n = 47). l1 and l2 of astral microtubules were measured as depicted on the illustration, using Fiji software. **(C)** Relative fluorescence intensities of astral microtubules ($I_{astral,\ rel}$) in siRNA-transfected cells (si-Control n = 31; si-ANXA1#1 n = 46; si-ANXA1#2 n = 47). Fluorescence intensities on the spindle ($I_{spindle}$) and total cell (I_{total}) were measured as depicted on the illustration, using Fiji software. **(D)** Ratio of pole-to-cortex distance (d) in siRNA-transfected cells (si-Control n = 31; si-ANXA1#1 n = 46; si-ANXA1#2 n = 47). Pole-to-cortex distance d1 and d2 were measured as depicted on the illustration, using Fiji software. **(E)** Confocal images of representative metaphase MCF-10A cells transfected with si-Control, si-ANXA1#1 or si-ANXA1#2 stained for F-actin (grey) and counterstained with DAPI (DNA, magenta). Insets show magnified images of framed regions. **(F)** Cortical to cytoplasmic ratio of actin fluorescence intensities ($I_{cortex}/I_{cytoplasm}$) in siRNA-transfected cells (si-Control: n = 30; si-ANXA1#1: n = 30; si-ANXA1#2 n = 30). Fluorescence intensities in the cytoplasm ($I_{cytoplasm}$) and total cell (I_{total}) were measured as depicted on the illustration, using Fiji software. **(G)** Confocal images of representative MCF-10A cells treated with DMSO (Control) or 1 μM Latrunculin A for 30 min, stained for F-actin (grey) and counterstained with DAPI (DNA, magenta). **(H)** Confocal images of representative MCF-10A cells treated with DMSO (Control) or 1 μM Latrunculin A for 30 min, stained for ANXA1, LGN, NuMA or p150^{Glued} (grey), and counterstained with DAPI (DNA, magenta). **(I)** Average cortical and cytoplasmic fluorescence intensity profiles of ANXA1, LGN, NuMA and p150^{Glued} from metaphase cells (Control: n = 30; Latrunculin A: n = 30). Asterisks indicate the spindle poles. All data are presented as means ± s.e.m. from 3 independent experiments. * $P \leq 0.05$, ** $P \leq 0.01$, *** $P \leq 0.001$, n.s. (not significant) (one-way ANOVA). All scale bars, 5 μm.

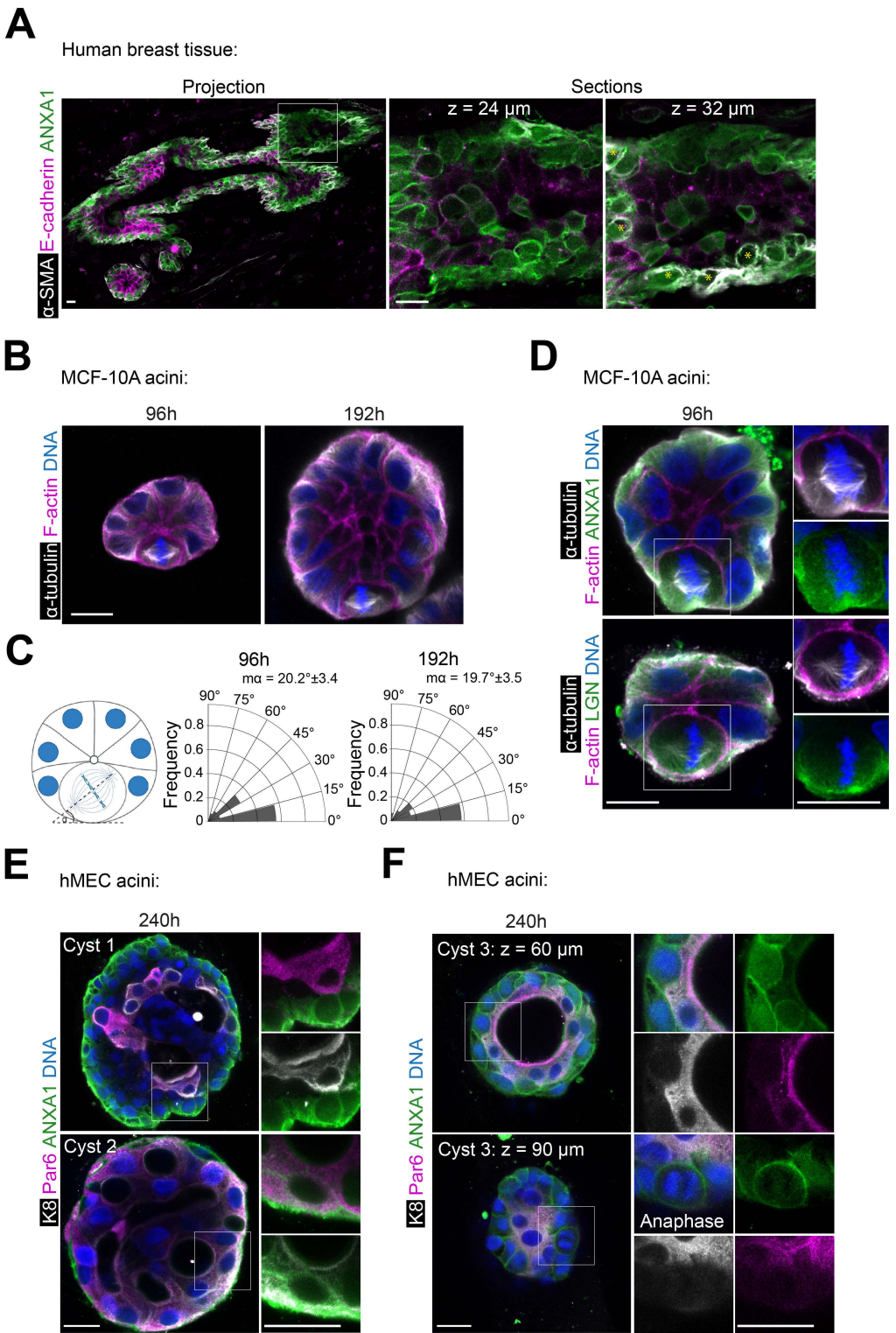
A
Human breast tissue:
Projection
Sections
z = 24 µm
z = 32 µm
α-SMA E-cadherin ANXA1
B
MCF-10A acini:
96h
192h
α-tubulin F-actin DNA
C
96h
mα = 20.2°±3.4
192h
mα = 19.7°±3.5
Frequency
90° 75° 60° 45° 30° 15° 0°
0 0.2 0.4 0.6 0.8
D
MCF-10A acini:
96h
α-tubulin F-actin ANXA1 DNA
α-tubulin F-actin LGN DNA
E
hMEC acini:
240h
Cyst 1
Cyst 2
K8 Par6 ANXA1 DNA
F
hMEC acini:
240h
Cyst 3: z = 60 µm
Cyst 3: z = 90 µm
Anaphase
K8 Par6 ANXA1 DNA

Fig S5. Characterisation of ANXA1 expression and localisation and OCDs in human mammary epithelial cells *in situ* and 3D culture. (A) Confocal images of representative human healthy breast cryosections (50 µm-thick) stained for ANXA1 (green), α-SMA (grey) and E-cadherin (magenta). **(B)** Confocal images of representative MCF-10A acini stained for F-actin (magenta) and α-tubulin (grey), and counterstained with DAPI (DNA, blue). **(C)** Spindle angle frequencies and mean angles (mα) (96h: n = 30 acini; 192h: n = 30 acini). **(D)** Confocal images of representative MCF-10A acini stained for F-actin (magenta), α-tubulin (grey) and LGN or ANXA1 (green), and counterstained with DAPI (DNA, blue). **(E)** Confocal images of representative hMEC acini forming multiple small lumens, stained for Par6 (magenta), K8 (grey) and ANXA1 (green), and counterstained with DAPI (DNA, blue). **(F)** Confocal images of representative hMEC acini forming a single central lumen, stained for Par6 (magenta), K8 (grey) and ANXA1 (green), and counterstained with DAPI (DNA, blue). All scale bars, 10 µm.

Fiji custom macro for quantification of cortical protein fluorescence intensities during prometaphase

```
macro elliptic_slicing {

//number of points to measure along the cell perimeter
k=180;
//length (in pixels) of the line for each measure:
px=15;
//starting position of the scan line relative to the ellipses long axis
S=90;

titre=getTitle();
getDimensions(x,y,nb_channel,o,t);
run("Set Measurements...", "area mean standard min bounding fit redirect=None decimal=3");
b=57.29578;
m=nResults;
IJ.deleteRows(0, m-1);
getPixelSize(unit, pw, ph, pd);
P=pd/pw;
run("Properties...", "unit=pixel pixel_width=1.0000 pixel_height=1.0000 voxel_depth="+(P)+"
origin=0,0");

		selectWindow(titre);
		run("Set... ", "zoom=150");
		setTool("Freehand");

//message prompting the user to set the ellipse:
		title = "cell center";
		msg = "use the Freehand tool to draw\n the cell's perimeter\n select the best z-
level\n then click \"OK\".";
		waitForUser(title, msg);

//measuring the ellipses center and size:
		run("Fit Ellipse");
		run ("Measure");
		x0=getResult("BX", (0));
		x1=getResult("Width", (0));
				M=getResult("Major", (0));
				m=getResult("Minor", (0));
				a=getResult("Angle", (0));
				E=sqrt(M*M-m*m)/M;
		y0=getResult("BY", (0));
		y1=getResult("Height", (0));
	//center of the ellipse:
		X0=x0+x1/2;
		Y0=y0+y1/2;

xx=newArray(k);
yy=newArray(k);

	for (i=0; i<k; i++) {
	xx[i]=(i);
	l=(360*i/k-a+S)/b;
```

```
        L=(360*i/k+S)/b;
        dia=sqrt(m*m/(1-E*E*cos(L)*cos(L)))/2;
                n1=dia-px/2;
                n2=dia+px/2;
        selectWindow(titre);
        makeLine(X0+n1*cos(l), Y0+n1*sin(l), X0+n2*cos(l), Y0+n2*sin(l));
                        run ("Measure");
                        yy[i]=getResult("Max", (0));
                        IJ.deleteRows(0, 0);
        print(yy[i]);
        };
Plot.create("plot1", "X", "Y", xx, yy);
}
```

Supplementary movie description

Movie S1

Description: LGN spatiotemporal distribution in control cells. Clonal MCF-10A cells stably expressing GFP-LGN were transfected with si-Control RNA for 72h and treated with Hoechst as described in the Methods. Images corresponding to 30 planes spaced by 0.6 μm through the cell volume were collected every 3 min as described in the Methods. Maximum intensity projections of GFP-LGN (green) and Hoechst (DNA, magenta) are shown through time. Time in min format and scale bar = 5 μm.

Movie S2

Description: ANXA1 knockdown impairs the dynamics of LGN and results in its unilateral distribution at the cortex. Clonal MCF-10A cells stably expressing GFP-LGN were transfected with si-ANXA1#1 RNA for 72h and treated with Hoechst as described in the Methods. Images corresponding to 40 planes spaced by 0.6 μm through the cell volume were collected every 3 min as described in the Methods. Maximum intensity projections of GFP-LGN (green) and Hoechst (DNA, magenta) are shown through time. Time in min format and scale bar = 5 μm.

Movie S3

Description: ANXA1 knockdown impairs the dynamics of LGN and results in its central distribution at the cortex. Clonal MCF-10A cells stably expressing GFP-LGN were transfected with si-ANXA1#1 RNA for 72h and treated with Hoechst as described in the Methods. Images corresponding to 40 planes spaced by 0.6 μm through the cell volume were collected every 3 min as described in the Methods. Maximum intensity projections of GFP-LGN (green) and Hoechst (DNA, magenta) are shown through time. Time in min format and scale bar = 5 μm.

Movie S4

Description: ANXA1 knockdown impairs the dynamics of LGN and results in its circumferential distribution at the cortex. Clonal MCF-10A cells stably expressing GFP-LGN were transfected with

si-ANXA1#1 RNA for 72h and treated with Hoechst as described in the Methods. Images corresponding to 40 planes spaced by 0.6 μm through the cell volume were collected every 3 min as described in the Methods. Maximum intensity projections of GFP-LGN (green) and Hoechst (DNA, magenta) are shown through time. Time in min format and scale bar = 5 μm.

Movie S5

Description: Mitotic spindle and chromosome dynamics in control cells. MCF-10A cells were transfected with si-Control RNA for 72h and treated with SiR-tubulin and Hoechst as described in the Methods. Images corresponding to 30 planes spaced by 0.6 μm through the cell volume were collected every 2.5 min as described in the Methods. Maximum intensity projections of SiR-tubulin (green) and Hoechst (DNA, magenta) are shown through time. Time in min format and scale bar = 5 μm.

Movie S6

Description: ANXA1 knockdown impairs mitotic progression and results in chromosome bridges during anaphase and telophase. MCF-10A cells were transfected with si-ANXA1#1 RNA for 72h and treated with SiR-tubulin and Hoechst as described in the Methods. Images corresponding to 40 planes spaced by 0.6 μm through the cell volume were collected every 2.5 min as described in the Methods. Maximum intensity projections of SiR-tubulin (green) and Hoechst (DNA, magenta) are shown through time. Time in min format and scale bar = 5 μm.

Movie S7

Description: ANXA1 knockdown impairs mitotic progression and results in misaligned small mitotic spindles. MCF-10A cells were transfected with si-ANXA1#1 RNA for 72h and treated with SiR-tubulin and Hoechst as described in the Methods. Images corresponding to 40 planes spaced by 0.6 μm through the cell volume were collected every 2.5 min as described in the Methods. Maximum intensity projections of SiR-tubulin (green) and Hoechst (DNA, magenta) are shown through time. Time in min format and scale bar = 5 μm.

Movie S8

Description: ANXA1 knockdown impairs mitotic progression and results in misaligned multipolar mitotic spindles. MCF-10A cells were transfected with si-ANXA1#1 RNA for 72h and treated with SiR-tubulin and Hoechst as described in the Methods. Images corresponding to 40 planes spaced by 0.6 μm through the cell volume were collected every 2.5 min as described in the Methods. Maximum intensity projections of SiR-tubulin (green) and Hoechst (DNA, magenta) are shown through time. Time in min format and scale bar = 5 μm.